International Journal of Rock Mechanics & Mining Sciences 139 (2021) 104580

Contents lists available at ScienceDirect

International Journal of Rock Mechanics and Mining Sciences

journal homepage: http://www.elsevier.com/locate/ijrmms

Modelling advective gas flow in compact bentonite: Lessons learnt from different numerical approaches

E. Tamayo-Mas [a,*], J.F. Harrington [a], T. Brüning [b], H. Shao [b], E.E. Dagher [c], J. Lee [d], K. Kim [e], J. Rutqvist [e], O. Kolditz [f], S.H. Lai [g], N. Chittenden [h], Y. Wang [i], I.P. Damians [j], S. Olivella [j]

[a] British Geological Survey, Keyworth, Nottingham, NG12 5GG, United Kingdom
[b] Federal Institute for Geosciences and Natural Resources, Hanover, Germany
[c] Canadian Nuclear Safety Commission/University of Ottawa, Ottawa, Ontario, Canada
[d] Korea Atomic Energy Research Institute, Daejeon, Republic of Korea
[e] Lawrence Berkeley National Laboratory, Berkeley, CA, USA
[f] Helmholtz Centre for Environmental Research, Leipzig, Germany
[g] Center for Advanced Model Research Development and Applications, National Central University, Taoyuan, Taiwan
[h] Quintessa Ltd, Henley-on-Thames, Oxfordshire, United Kingdom
[i] Sandia National Laboratories, Albuquerque, NM, USA
[j] Universitat Politècnica de Catalunya, Barcelona, Spain

ARTICLE INFO

Keywords:
Gas flow
Dilation
Two-phase models
Mechanical deformation
Continuous approaches
Fractures

ABSTRACT

In a repository for radioactive waste hosted in a clay formation, hydrogen and other gases may be generated due to the corrosion of metallic materials under anoxic conditions, the radioactive decay of waste and the radiolysis of water. If the gas production rate exceeds the gas diffusion rate within the pores of the clay, a discrete gas phase will form and accumulate until its pressure becomes large enough to exceed the entry pressure of the surrounding material, at which point dilatant, advective flow of gas is expected to occur.

The purpose of Task An under DECOVALEX-2019 is to better represent the processes governing the advective movement of gas in both low-permeability argillaceous repository host rocks and clay-based engineered barriers within numerical codes. In this paper special attention is given to the mechanisms controlling gas entry, flow and pathway sealing and their impact on the performance of the engineered clay barrier. Previous work suggests gas flow is accompanied by the creation of dilatant pathways whose properties change temporally and spatially within the medium. Thus, four new types of approaches have been developed: (i) standard two-phase flow models (continuous techniques) incorporating a range of different mechanical deformation behaviours, (ii) enhanced two-phase flow models in which fractures are embedded within a plastic material (continuous techniques) or incorporated into the model using a rigid-body-spring network (discrete approaches), (iii) a single-phase model incorporating a creep damage function in which only gas flow is considered, and (iv) a conceptual approach used to examine the chaotic nature of gas flow. The outputs from these different approaches are compared. This is an essential step as the choice of modelling approach strongly impacts the representation and prediction of gas flow in a future repository. In addition, experience gained through this task is of direct relevance to other clay-based engineering issues where immiscible gas flow is a consideration including hydrocarbon migration, carbon capture and storage, shale gas and landfill design.

This paper summarises the outcomes of work in Task A conducted between May 2016 and May 2019 and provides a brief overview of the experimental data and a synthesis of the work of the participating modelling teams.

* Corresponding author.
E-mail addresses: elena@bgs.ac.uk (E. Tamayo-Mas), jfha@bgs.ac.uk (J.F. Harrington), Torben.Bruening@bgr.de (T. Brüning), Hua.Shao@bgr.de (H. Shao), elias.dagher@canada.ca (E.E. Dagher), jwl@kaeri.re.kr (J. Lee), kunhwikim@lbl.gov (K. Kim), jrutqvist@lbl.gov (J. Rutqvist), olaf.kolditz@ufz.de (O. Kolditz), luckycvita.lai@gmail.com (S.H. Lai), neilchittenden@quintessa.org (N. Chittenden), ywang@sandia.gov (Y. Wang), ivan.puig@upc.edu (I.P. Damians), sebastia.olivella@upc.edu (S. Olivella).

https://doi.org/10.1016/j.ijrmms.2020.104580
Received 18 February 2020; Received in revised form 17 December 2020; Accepted 17 December 2020
Available online 2 February 2021

1. Introduction

In 1999, Rodwell et al. [1] stated "there are few problems in geoscience more complex than the quantitative prediction of gas migration fluxes through an argillaceous rock formation". To understand this statement, it is necessary to appreciate why argillaceous materials (which include clays, claystones and mudrocks) differ from other clastic sedimentary rocks. Key factors in this respect include the sub-microscopic dimensions of the interparticle spaces, the very large specific surface of the mineral phases, strong physico-chemical interactions between water molecules and surfaces, very low permeability, generally low tensile strength, a deformable matrix, and a very pronounced coupling between the hydraulic and mechanical response of these materials. It is therefore necessary to consider these properties collectively when defining the behaviour of these materials (both natural and engineered) in order to successfully represent gas flow in such systems.

With this in mind, the processes governing the movement of repository gases through engineered barriers and clay-rich host rocks can be split into two components, (i) molecular diffusion (governed by Fick's Law) and (ii) bulk advection. In the case of a repository for radioactive waste, corrosion of metallic materials under anoxic conditions will lead to the formation of hydrogen. Radioactive decay of the waste and the radiolysis of water are additional source terms. If the rate of gas production exceeds the rate of gas diffusion within the pores of the barrier or host rock, a discrete gas phase will form.[2,3,4] Under these conditions, gas will continue to accumulate until its pressure becomes sufficiently large for it to enter the surrounding material.

In clays and mudrocks, four primary phenomenological models describing gas flow can be defined, Fig. 1: (1) gas movement by diffusion and/or solution within interstitial fluids along prevailing hydraulic gradients; (2) gas flow in the original porosity of the fabric, commonly referred to as two-phase flow; (3) gas flow along localised dilatant pathways, which may or may not interact with the continuum stress field; and (4) gas fracturing of the rock similar to that performed during hydrocarbon stimulation exercises.

There is now a growing body of evidence[6,7,8–12,13–15] that in the case of plastic clays and in particular bentonite, classic concepts of porous medium two-phase flow are inappropriate and continuum approaches to modelling gas flow may be questionable, depending on the scale of interest, the scale of the processes and resolution of the numerical model. However, the detail of the dilatant mechanisms controlling gas entry, flow and pathway sealing are unclear as is the extent to which the "memory" of such features within clay may impair barrier performance, in particular, acting as preferential flow paths for the movement of radionuclides transported in the gas phase.

Several international projects aiming to understand the advective movement of gas through clay-rich materials have already been conducted. These include MEGAS (1991–1994), EVEGAS (1994–1996), PROGRESS (1996–1999), GAMBIT (1998–2005), NF-Pro (2002–2006) and FORGE (2009–2013), see Bond et al.[16] for more details. However, development of new and novel numerical representations for the quantitative treatment of gas in clay-based repository systems are required, and are the primary focus of Task A in the DECOVALEX-2019 project. New numerical techniques provide an invaluable tool with which to assess the impact of gas flow on repository layout and therefore design of any future facility. In addition, the same processes and mechanisms described in such models are of direct relevance to other clay-based engineering issues where immiscible gas flow is involved e.g. shale gas, hydrocarbon migration, carbon capture and storage and landfill design.

Task A is organised into three steps, starting with code development (step 0), followed by modelling of a 1D gas flow test (step 1) and a spherical gas flow test (step 2). An optional step (step 3), dealing with natural argillaceous materials, was also introduced but only modelled by UPC/Andra, see Damians et al.[17] for more details. The reason to include both experiments is to verify the capabilities of the codes to numerically represent the complex coupled multi-phase flow problem, since it is not possible to build confidence from a single test.

This paper gives a technical overview and synthesis of key conclusions of work conducted from May 2016 to May 2019 by the participating modelling teams:

1. BGR/UFZ (Germany): Federal Institute for Geosciences and Natural Resources and the Helmholtz Centre for Environmental Research.
2. CNSC (Canada): Canadian Nuclear Safety Commission.
3. KAERI (Korea): Korea Atomic Energy Research Institute.
4. LBNL (United States of America): Lawrence Berkeley National Laboratory.
5. NCU/TPC (Taiwan): National Central University and Taiwan Power Company (Taipower).
6. Quintessa/RWM (United Kingdom): Quintessa Ltd on behalf of Radioactive Waste Management.
7. SNL (United States of America): Sandia National Laboratories.
8. UPC/Andra (Spain/France): Universitat Politècnica de Catalunya, funded by l'Agence nationale pour la gestion des des déchets radioactifs.

Further details can be found in other synthesis publications, see Tamayo-Mas et al.[18,19].

2. Experimental data

In this task, two different experiments undertaken by the British Geological Survey (BGS) were used: (a) a one-dimensional and (b) a three-dimensional gas injection test. Both tests were performed on compacted bentonite samples supplied by Clay Technology AB (Lund, Sweden) and were comprised of two stages; hydration followed by gas testing.

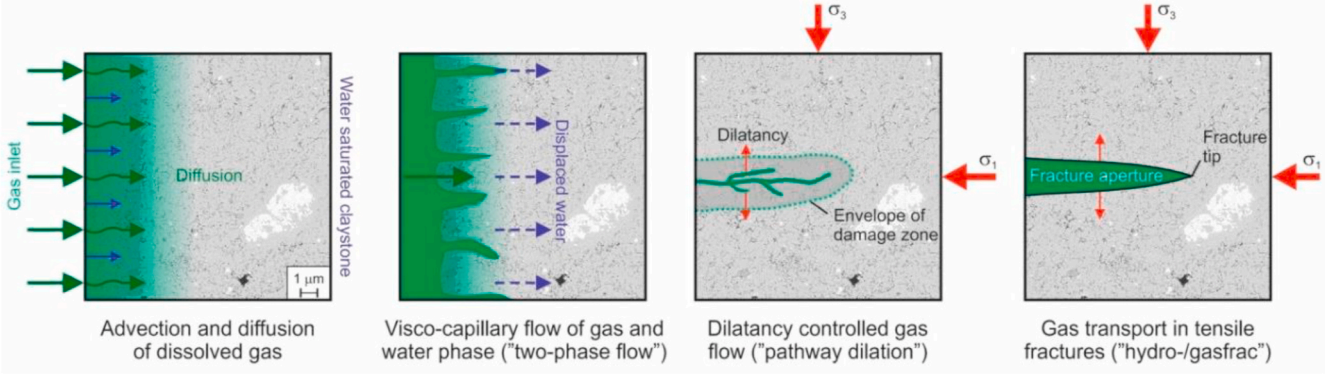

Fig. 1. Conceptual models of gas flow (after Marschall et al.[5] BGS © UKRI).

2.1. One-dimensional gas flow test on saturated bentonite

The first experiment was performed on a pre-compacted Mx80 bentonite sample, see Table 1 for the sample dimensions and geotechnical parameters and Daniels and Harrington[20] for a detailed description of the sample preparation and laboratory procedure.

As reported by Daniels and Harrington[20]; a constant volume pressure vessel was used for the testing (see Fig. 2 and Harrington and Horseman[10] for a general description of the employed apparatus). The pressure vessel was instrumented with (i) 2 axial and 3 radial load cells, (ii) 3 radial arrays, which allowed the continuous monitoring of pore pressure within each array, and (iii) a central filter mounted at the end of a 6.4 mm diameter steel tube inserted into the sample.

Equilibration phase started immediately after installation of the sample, with water uptake from the radial and backpressure end closure filters. This stage ran for a period of 7.3 days. Once sufficient swelling pressure had been established, the hydration phase was initiated by simultaneously applying an external pore pressure of 1.0 MPa, up to day 39.3, see Fig. 3.

In phase 2, gas was injected across the axial end face of the cylindrical sample, through filter EC1, and outflow was measured at the opposing end, see report by Daniels and Harrington[20] for a detailed description. This began on day 39, when additional helium was added to the injection system to increase gas pressure to 3 MPa. This was then held constant for a period of 7 days. At day 46, the injection pump was set to a constant gas compression rate of 500 μl/h and the injection pressure gradually increased for the next 8 days from 3 MPa to 5 MPa whilst the volume of gas in the injection system decreased from 235 ml to 139.7 ml. At this point (day 54), the gas compression rate was reduced to 375 μl/h. At day 61, 59.95 ml further helium was added to the interface vessel, whilst maintaining constant gas pressure in the system. See Fig. 4 for the evolution of total stresses and pore pressures before gas breakthrough.

Gas breakthrough (defined as the emergence of gas at backpressure filter) occurred at 63.8 days. At day 71, after a period of gas flow through the sample, the injection pump was stopped. Between day 71 and day 76, the pore pressures decreased substantially, see Fig. 5a.

Examination of the axial and radial load cell data during gas entry and breakthrough, Fig. 5, indicates that stress within the sample increased at the same time as gas breakthrough occurred in the backpressure filter. Following gas breakthrough, the system approached a quasi-steady state as gas pressure approached an asymptote and flow in and out of the system began to converge (between days 63.5 and 71), Fig. 5b. Following gas breakthrough, total stress and pore pressure appeared integrally linked to the gas pressure within the clay. This is in line with previous observations.[10,11] This continued following the cessation of pumping, as gas pressure and total stress and pore pressure began to decay. During this phase of testing, gas outflow was sporadic suggesting new gas pathways continued to open and close during this phase of testing. Some of these outflow events correlated with observed changes in total stress and pore pressure, while others did not.

2.2. Spherical gas flow test through saturated bentonite

The second experiment consisted of a 3D gas injection test performed on another pre-compacted Mx80 bentonite sample, see Table 2 for the basic geotechnical properties. A complete description of sample preparation can be found in Harrington et al.[11].

The test comprised a series of component phases designed to understand the response of the sample during gas entry and breakthrough. At the outset, the test was configured with helium gas within the central injection filter. Pressure in the central injection filter and backpressure systems were initially set at 0.25 MPa. At day 8.3, injection and backpressures were increased to 1.0 MPa (in all filters except the backpressure) to reduce swelling time and promote quicker hydration of the clay. This pressure was then maintained in all radial filters for the rest of the test. A time-dependent development of swelling pressure was observed. A mass balance of the system demonstrates that around 1.45 ml of water was injected into the sample between 0 and 23 days when stress begins to stabilise. Geotechnical measurements based on the post-test mass of the sample indicate a water saturation in excess of 99%. This measurement was made after prolonged gas testing indicating that the sample must have been fully saturated at day 49, yielding an average stress of 6.8 MPa and a swelling pressure of 5.8 MPa. It also suggests that the volume of the gas pathways (i.e. the gas saturations) must remain small throughout the experiment.

Gas testing began on day 49. For the purposes of the DECOVALEX project, numerical modelling of the data began from day 735 of the test, following the slow incremental increase of gas pressure within the injection filter over the previous 700-day period. This comprised a series of pressure steps of varying duration to examine if gas could advect at pressures significantly lower than the sum of the average swelling and backpressure values, see Harrington et al.[11] for more details.

At day 735, pressure in the injection system was slowly increased by compressing the gas at a constant rate of 125 μl/h, Fig. 6. At day 739.2, gas pressure exceeded the minimum measured stress (i.e. axial stress A1, see Fig. 2). However, it is not until day 743.5, when gas pressure exceeds the maximum measured stress (radial stress R2, see Fig. 2), that a coupling between gas pressure and stress becomes evident, signified by the change in slope of the stress response.[1] As gas pressure continued to slowly increase, all stress sensors exhibit a positive gradient, slowly increasing with gas pressure. The first clear evidence for gas entry occurs at day 747.3 when variance in absolute stress values within the bentonite increased or decreased as a function of time. This somewhat chaotic behaviour in the stress field is thought to relate to specific pathway propagation events as gas penetrates and migrates through the clay, with the magnitude and direction of the stress change strongly linked to the orientation and aperture of the pathway.[11,21] In this way, each inflection in the gas pressure and stress traces would seem to relate to changes in the geometric configuration of gas pathways as a function of time. This yields a gas entry pressure around 8.05 MPa, which is in line with previous values reported by Graham et al.[8] Inspection of the data in Fig. 6 indicates abrupt changes in stress are often associated with specific discharge events to one or more of the three radial filter arrays. These outflows are both sporadic and non-uniformly distributed through the clay, indicating localised flow through initially unstable pathways, which open and close depending on the local value of gas pressure and stress in the system. This capacity for closure and rapid reduction in outflow highlights the ability of the clay to self-seal under these circumstances.

This instability in pathway geometry leads to an under-development of gas permeability (i.e. the instantaneous permeability within the sample is inadequate to allow the passage of gas at the prescribed injection rate), constricting flow, which then results in continued gas pressurisation. While a number of minor breakthrough events occur, it is not until day 756.9, at an initial peak gas pressure of 9.72 MPa, that major gas breakthrough finally occurs. This is accompanied by rapid degassing of the clay through arrays 1 and 2, resulting in a negative pressure transient to a new gas pressure of 9.29 MPa. Thereafter, gas pressure continues to decline at a slower rate as outflow continues, reaching a minimum value of 9.02 MPa at day 757.4. The inability of these previously conductive pathways to remain open results in a lack of permanent permeability change within the clay, leading to two further discrete gas breakthrough events at days 761 and 764. Inspection of the data shows multiple inflections in stress and outbursts of gas during the second pressurisation event from day 757–761.

Following the third major gas breakthrough event at day 764, outflows to arrays 1 and 2 reduce with flow now focussed to array 3. This

[1] Given gas is present in axial filters EC1 and EC2 it is not possible to accurately determine porewater pressure, and therefore, the effective stress.

Table 1
Basic physical properties of sample Mx80-D prior to testing. An assumed specific gravity for the mineral phases of 2.77 Mg m^{-3} and a density of water of 1000 kg/m^3 (Horseman and Harrington)[14] was used in these calculations. Geotechnical properties are based on oven drying of material at 105 °C testing.

Sample	Length (mm)	Diameter (mm)\	Moisture content	Dry density (kg/m^3)\	Porosity	Saturation
Mx80-D	119.90	59.69	0.266	1.579	0.430	97.8

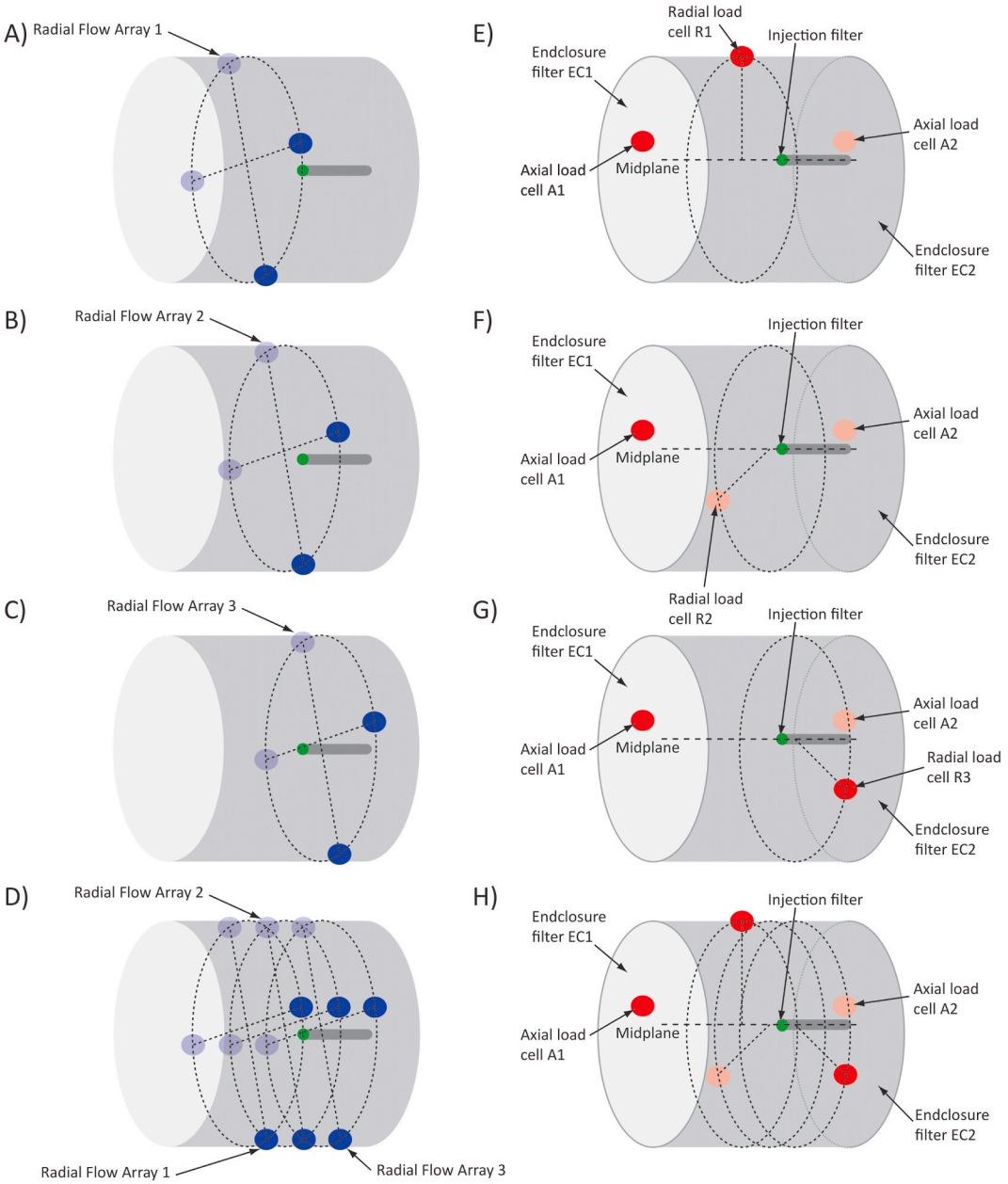

Fig. 2. Schematic representation of the test system. Images [A] through [D] show the location of the end-closure (EC) and filter arrays, while images [E] through [H] show the location of the load cells used for the measurement of stress.

phase of the test is accompanied by an apparent reduction in pathway propagation events signified by minimal perturbation of the stress field, exhibited by a much smoother trace. In addition, stresses are seen to generally converge, with the exception of that measured nearest the A1 end-closure, which continues to maintain a significant offset to the rest of the stress data. As gas pressurisation continues from day 765 onwards, Fig. 7, outflow to array 3 varies, spiking again at day 767.8, which is accompanied by an inflection in the gas injection pressure. However, as before, the pathway is unable to remain open, permeability drops and gas pressurisation continues. Gas pressure peaks at 9.88 MPa around day 771.7, with flow continuing to be focussed to array 3, Fig. 7. This is followed by a protracted negative pressure transient leading to a quasi-steady state by around day 825. During this period, the change in injection pressure is crudely mirrored in all of the stress sensors, which exhibit none of the chaotic patterns observed with earlier breakthrough events. Gas pressure is now roughly equal to the maximum value of stress in the system. While outflow remains focussed to one specific array, the flux remains relatively stable, exhibiting much less variability

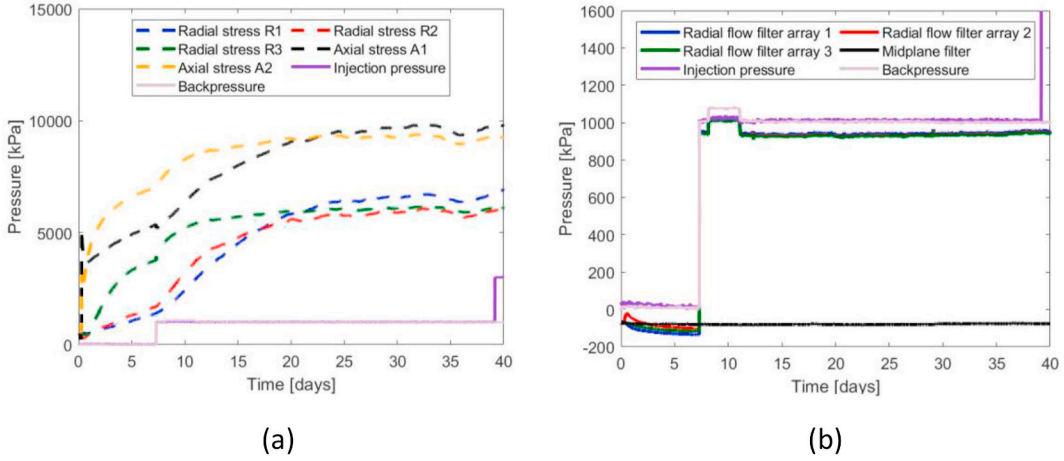

Fig. 3. Experiment 1 (equilibration and hydration phases): (a) swelling pressure measured by the axial and radial load cells, injection pressure and backpressure; (b) axial and radial pore pressure.

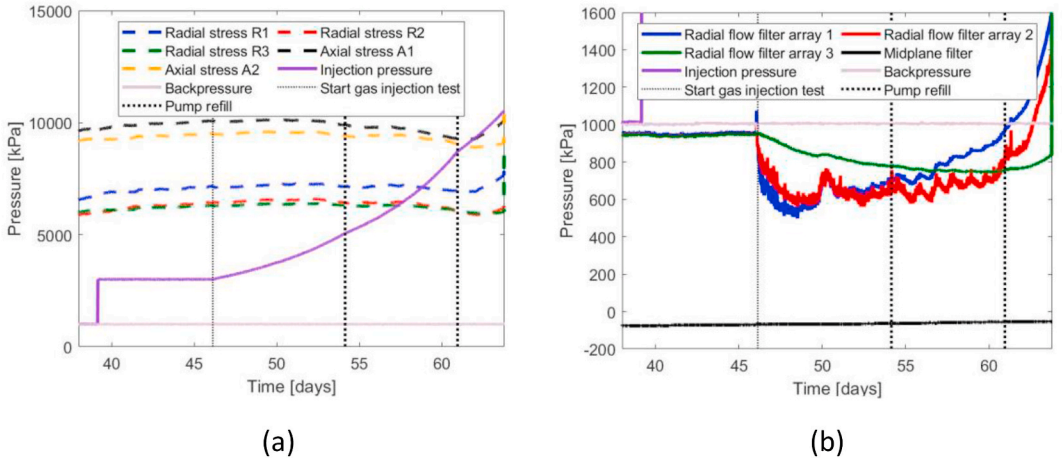

Fig. 4. Experiment 1 (up to gas breakthrough at 63.8 days): (a) total stresses and (b) pore pressures.

than before. Outflow to arrays 1 and 2 remain minimal (less than 1.0×10^{-10} m^3/s), indicating highly localised gas flow within the bentonite sample.

3. Modelling approaches

Different modelling approaches have been developed (see summary Tables 3 and 4) through back-analysis of data: (a) two-phase flow models, where the basic physical principles such as mass and momentum balance are coupled to different mechanical deformation behaviours; (b) enhanced-two phase flow models, in which embedded or discrete fractures are included, (c) a single-phase flow model, where gas permeability evolution is captured by processes representing capillary opening/closing and permeability includes a micro-scale deformation ('creep') process and (d) a conceptual chaotic model that places special emphasis on the capture of dilatancy. Two of these approaches (CNSC-PD and UPC/Andra-ED) include heterogeneity: the former applies a spatially random normal distribution to the initial porosity material property with a mean porosity set of 0.44 and a standard deviation of 0.01; the latter selects a random initial permeability field, see Appendix A.2 for more details.

3.1. Classical two-phase flow models coupled to mechanical deformation

Four classical two-phase flow models (BGR/UFZ-E, CNSC-PD, KAERI-D and NCU/TPC-V), where basic physical principles such as mass and momentum balance apply for each phase, have been developed. These standard models have been coupled to different mechanical deformation behaviours and have significantly altered water retention curves, relative permeability curves and/or intrinsic permeability dependencies in order to better represent the experimentally observed features.

BGR/UFZ adopted a continuous two-phase flow approach that considers water and gas in an elastically deformable porous medium. Water is considered to be incompressible whereas gas, assumed to behave as an ideal gas, is compressible. Hence, the standard mass balance equations for the water phase

$$\frac{\partial \varphi \rho_w S_w}{\partial t} + \varphi \rho_w S_w \nabla \cdot \frac{\partial \mathbf{u}}{\partial t} + \nabla \mathbf{q}_w = 0 \quad (1)$$

and the gas phase

$$\frac{\partial \varphi \rho_g (1 - S_w)}{\partial t} + \varphi (1 - S_w) \rho_g \nabla \cdot \frac{\partial \mathbf{u}}{\partial t} + \nabla \mathbf{q}_g = 0 \quad (2)$$

are solved, where φ (−) is the porosity of the medium, ρ_w (kg/m^3) and ρ_g (kg/m^3) stand for the density of water and gas respectively, S_w (−) is the water saturation, $\mathbf{q}_w$ (kg/m^2·s) and $\mathbf{q}_g$ (kg/m^2·s) are the flow velocity of water and gas respectively (described by the modified Darcy's law) and $\mathbf{u}$ (m) is the displacement vector. Note that due to gas compressibility,

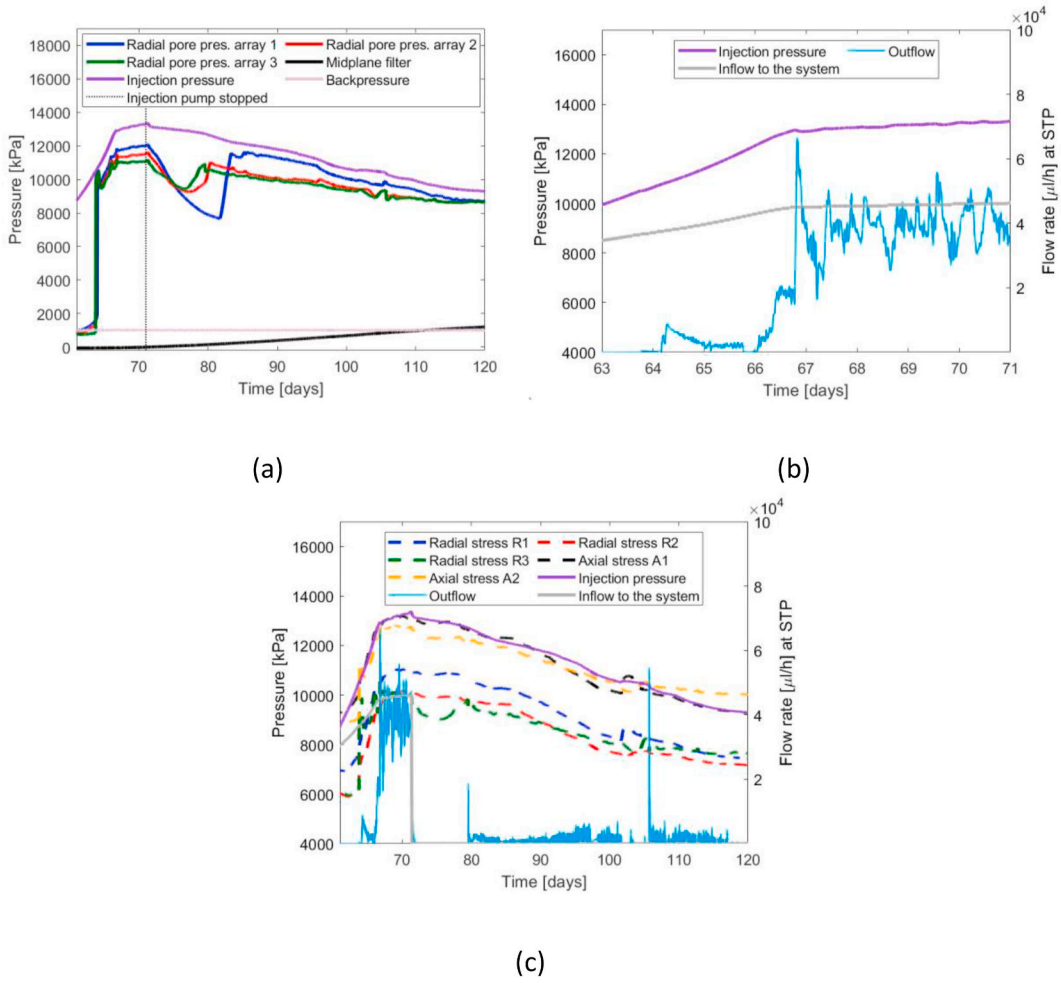

Fig. 5. Experiment 1 (gas phase, from day 61 to day 121): (a) injection pressure, backpressure and radial pore pressure transducer data and (c) total stress and flow data. Standard temperature and pressure (STP) are defined as 273.15 K and 101.325 kPa respectively. Note that 'Inflow' is the gas compression rate within the injection system rather than gas inflow into the sample. In (b) a zoom-in (from day 63–71) is plotted.

Table 2
Basic physical properties of sample Mx80-A prior to testing. An assumed specific gravity for the mineral phases of 2.77 Mg m^{-3} and a density of water of 1000 kg/m^3 (Horseman and Harrington)[14] was used in these calculations. Geotechnical properties are based on oven drying of material at 105 °C.

Sample	Length (mm)	Diameter (mm)	Moisture content	Dry density (kg/m^3)	Porosity	Saturation
Mx80-A	121.36	59.76	0.266	1.560	0.437	95.0

gas density depends on gas pressure and temperature. These equations are coupled to the momentum balance equation

$$\nabla\left[\boldsymbol{\sigma}' - \alpha\left(p_g - S_w p_c\right)\mathbf{I}\right] + \rho\mathbf{g} = 0 \tag{3}$$

where $\boldsymbol{\sigma}'$ (Pa) is the effective stress tensor, α (−) is the Biot coefficient,[22] p_g (Pa) is the gas pressure, p_c (Pa) is the capillary pressure, $\mathbf{I}$ is the identity tensor, ρ (kg/m^3) is the total density and $\mathbf{g}$ is the gravitational acceleration (m/s^2). The capillary pressure is here described by the van Genuchten model [23] and hence,

$$p_c = p_g^{entry}\left(S_{ec}^{\frac{m}{1-m}} - 1\right)^{\frac{1}{m}} \tag{4}$$

where m (−) is a material parameter, S_{ec} (−) is the effective saturation and p_g^{entry} (Pa) is the gas entry pressure. The Mualem model [24] is used to describe the water and gas relative permeabilities thus leading to

$$k_{r,w} = S_{ec}^{\frac{1}{2}}\left[1 - \left(1 - S_{ec}^{\frac{m}{m-1}}\right)^{\frac{m-1}{m}}\right]^2 \tag{5}$$

$$k_{r,g} = (1 - S_{ec})^{\frac{1}{2}}\left(1 - S_{ec}^{\frac{m}{m-1}}\right)^{2(1-1/m)} \tag{6}$$

The pressure-dependent permeability relationship

$$\mathbf{k} = f(p_g) = \begin{cases} (1 + a p_g)\mathbf{k}_{int}, & p_g \le p_{crit} \\ \left(b(p_g - p_{crit}) + 1 + a p_{crit}\right)\mathbf{k}_{int}, & otherwise \end{cases} \tag{7}$$

already used to simulate other gas migration tests, see for instance

[2] This value will be set to 1 MPa and its impact will be assessed in Dagher E. E., Nguyen T.S. and Infante Sedano J.A. Assessing Mechanisms of Mechanical Deformation to Simulate Two-Phase Flow in a Swelling Geomaterial. (To be submitted to the Special Publication of International Journal of Rock Mechanics and Mining Sciences).

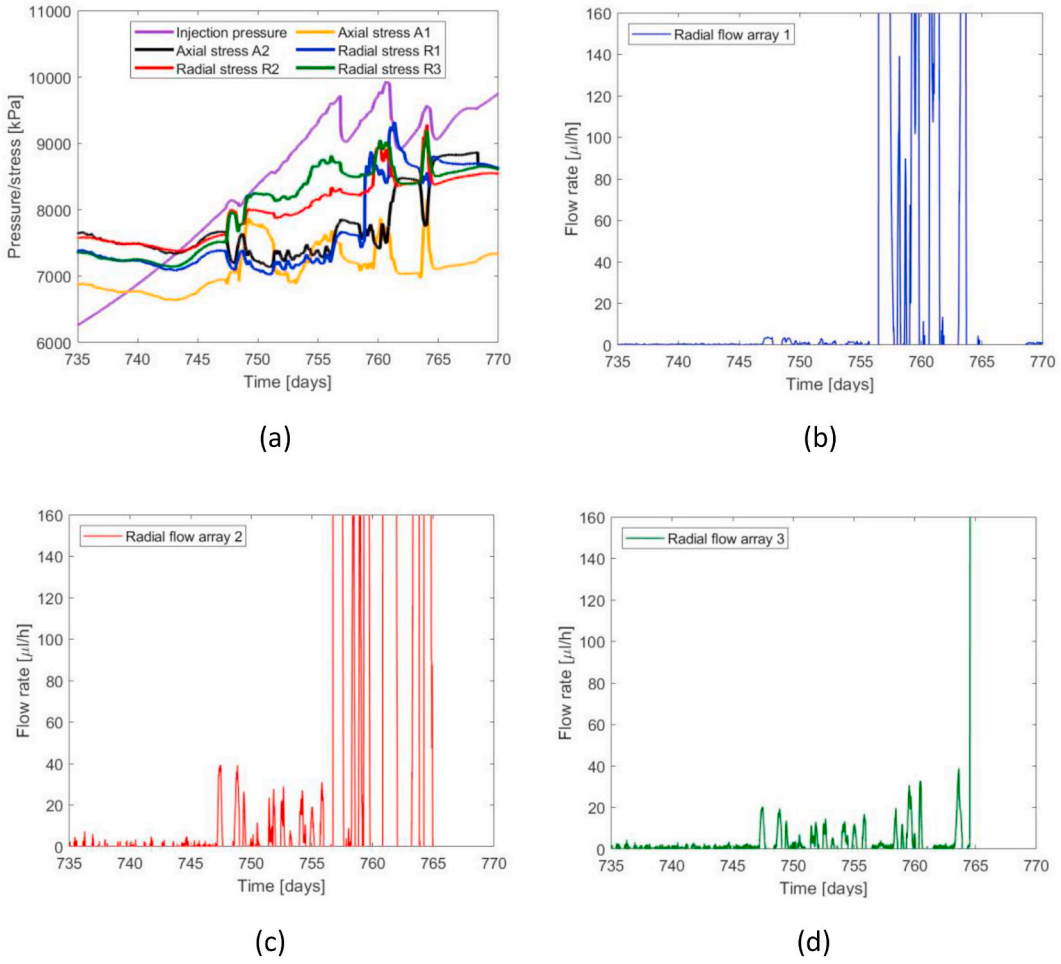

Fig. 6. Experiment 2: evolution in gas pressure, stress and outflow during multiple gas breakthrough events. (a) Gas pressure and local stress. (b–d) outflow of gas to radial arrays 1, 2 and 3 respectively. Outflow data is time-averaged to help identify underlying trends. This introduces a small time-shift in the data of ±3 h which explains why outflow appears to occur marginally before peak gas pressures.

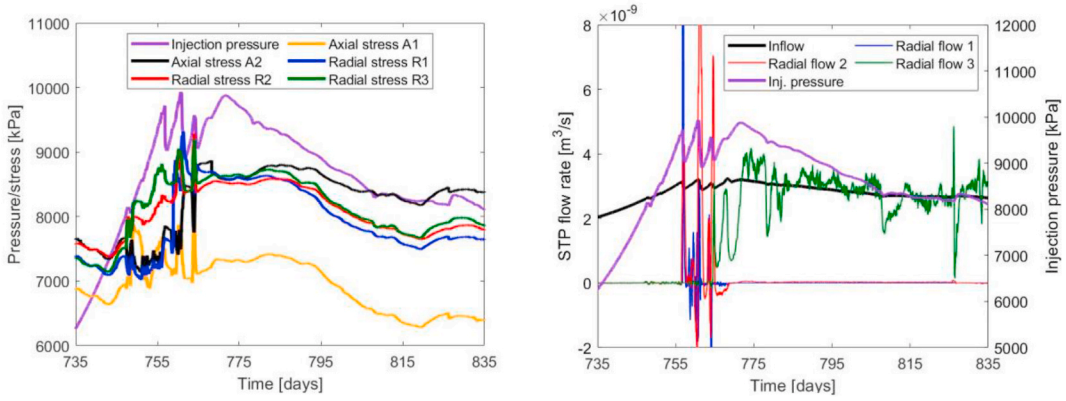

Fig. 7. Experiment 2: (a) evolution in stress behaviour from initial gas entry to steady state conditions. The reduction in the variability of stress from day 768 onwards is accompanied by the development of 'stable' outflow conditions [b], with flux localised to one drainage array. See (c) for some details. Standard temperature and pressure (STP) are defined as 273.15 K, 101.325 kPa respectively. Note that 'Inflow' is the gas compression rate within the injection system rather than gas inflow into the sample.

Senger et al.[25] is used for the numerical simulations, where p_{crit} (Pa) is the critical value of gas pressure, $\mathbf{k}_{int}$ (m^2) is the intrinsic permeability tensor and a and b are calibrated constant parameters.

BGR/UFZ implemented the BGR/UFZ-E model using the OpenGeoSys (OGS) code.[26] To simulate the one-dimensional test (experiment 1), a triangular two-dimensional axi-symmetric mesh was used, whereas a hexahedral three-dimensional mesh was generated for the spherical test (experiment 2), see Appendix A.2 for more details.

A second two-phase hydro-mechanical model was developed by CNSC, the so-called CNSC-PD model. It also describes the hydraulic properties by using the Mualem-van Genuchten type analytical functions. The Millington and Quirk[27] model is applied to describe the

Table 3
Main properties of the modelling approaches that have been developed during the task (for both experiment 1 and experiment 2).

Model	Funding centre	Model type	Mechanical deformation	Hydraulic approach
BGR/UFZ-E	BGR/UFZ	continuous	elasticity	two-phase
CNSC-PD	CNSC	continuous	elastoplastic damage	two-phase
KAERI-D	KAERI	continuous	elastic damage model	two-phase
NCU/TPC-V	Taiwan Power Company	continuous	visco-elastic	two-phase
UPC/Andra-ED	ANDRA	continuous	elasticity with dilatancy	two-phase with embedded fracture
LBNL-D	US DOE	discontinuous	elastic damage and fractures	two-phase
Quintessa/RWM-ECap	RWM	continuous	elasticity	single-phase

Table 4
Main numerical features of the modelling approaches that have been developed during the task (for both stage experiment 1 and stage experiment 2). See Appendix A for more details. Note that FE stands for Finite Element, FD stands for Finite Difference and FV for finite volume.

Model	Test	Software	Space discretisation method	Number of calibrated parameters
BGR/UFZ-E	1,2	OpenGeoSys 5.8	FE	Not provided
CNSC-PD	1,2	COMSOL Multiphysics® 5.4	FE	25
KAERI-D	1	TOUGH2/FLAC3D	FD	5
	2	COMSOL Multiphysics®	FE	5
NCU/TPC-V	1,2	THMC 7.1	FE	7
UPC/Andra-ED	1,2	Code_bright 8.6	FE	11
LBNL-D	1,2	TOUGH-RBSN	FV	Not provided
Quintessa/RWM-ECap	1,2	QPAC 4.2	FV	12

diffusion of gas through water and both the intrinsic permeability and the soil-water characteristic curve are assumed to be porosity-dependent functions. For the intrinsic permeability, for instance, the Pall and Moshenin[28] model is used and it reads

$$k_{ij} = \frac{D_{vs}^2}{180}\frac{\varphi^3}{(1-\varphi)^2} \tag{8}$$

where D_{vs} (m) is the volume-surface mean diameter and φ (−) is the porosity (assumed to be a function of the volumetric strain). A specific feature of the model is that it includes compressibility due to changes in suction, pore-water pressure and pore-gas pressure. Moreover, Klinkenberg effects[29] due to slip flow of gas at pore walls are considered and thus

$$k_{ij_g} = k_{ij_w}\left(1+\frac{b}{p_g}\right) \tag{9}$$

where k_{ij_g} (m^2) is the gas specific intrinsic permeability, k_{ij_w} (m^2) is the liquid intrinsic permeability, p_g (Pa) is the pore-gas pressure and b (Pa) is the Klinkenberg factor.

This hydraulic model is coupled to a non-linear poro-elastoplastic damage model that uses a modified extended Barcelona Basic Model.[30]

In this model, a damage factor D accounting for both tensile and compressive damage components is included and influences the intrinsic permeability as well as the soil stiffness. The modified Bishop's effective stress principle[31] defined by Khalili and Khabbaz[32]; which is able to exhibit a self-healing behaviour, is also adopted and hence the effective pore pressure $\bar{p}$(Pa) reads

$$\bar{p} = (1-\chi)p_g + \chi p_w \tag{10}$$

where χ (−) is the effective stress parameter.

Model CNSC-PD is implemented in COMSOL Multiphysics®. To simulate the one-dimensional and the spherical tests, different triangular finite element meshes have been used: (i) a two-dimensional axisymmetrical mesh and (ii) a three-dimensional mesh, see Appendix A.2 for more details.

A third two-phase hydro-mechanical model (KAERI-D) was developed by KAERI. In KAERI-D, the classical multi-phase Darcy's law is solved and combined with a mass balance equation for each component. This model assumes a local thermodynamic equilibrium. Two components are present in each phase (water and gas) and a compositional model that allows a transfer of components from one phase into the other is assumed. This model does not include dispersion nor diffusion.

As given by Fall et al.[33]; this classical two-phase flow model is coupled to the elastic damage model proposed by Tang et al.[34] According to this model, the host rock is assumed to be brittle-elastic. That is, the stress-strain relationship is divided into an elastic phase (where no damage or irreversible damages occur) and a damage phase, that accounts for the deterioration of the rock (decrease of strength, rigidity and toughness, for instance). The effective stress tensor $\boldsymbol{\sigma}'$ (Pa) is thus defined as

$$\begin{aligned} &\textit{Before gas breakthrough(elastic model)}: \ \boldsymbol{\sigma}' = \mathbf{C}:\boldsymbol{\varepsilon} \\ &\textit{After gas breakthrough(damage model)}: \boldsymbol{\sigma}' = (1-D)\mathbf{C}:\boldsymbol{\varepsilon} \end{aligned} \tag{11}$$

where $\boldsymbol{\varepsilon}$ (−) is the infinitesimal strain tensor, $\mathbf{C}$ (Pa) is the fourth-order stiffness tensor, D (−) is the damage parameter and: is the double tensor contraction. As seen in Equation (11), the elastic modulus of the rock progressively degrades as damage grows. In fact, to include both the tension and the compression behaviours of the rock, two damage parameters are used. Hence, when the tensile stress in an element reaches its tensile strength, the tensile damage variable

$$D_t = \begin{cases} 0 & \varepsilon_{t_o} \le \varepsilon \\ 1-\dfrac{f_{tr}}{E_0\varepsilon} & \varepsilon_{t_u} \le \varepsilon \le \varepsilon_{t_o} \\ 1 & \varepsilon \le \varepsilon_{t_u} \end{cases} \tag{12}$$

is used, where f_{tr} (Pa) stands for the residual tensile strength, E_0 (Pa) is the initial (or undamaged) elastic modulus, ε (−) is the strain and ε_{t_o} (−), ε_{t_u} (−) are tensile strain limits. To describe deterioration under a compressive or shear stress condition (that is, when shear stress attains the strength criterion defined by the Mohr-Coulomb failure envelope), KAERI-D model uses the compressive damage parameter

$$D_c = \begin{cases} 0 & \varepsilon \le \varepsilon_{c_o} \\ 1-\dfrac{f_{cr}}{E_0\varepsilon} & \varepsilon_{c_o} \le \varepsilon \end{cases} \tag{13}$$

where f_{cr} (Pa) is the residual compressive strength, and ε_{c_o} (−) is a compressive strain limit.

This damage mechanism is also included when defining the intrinsic permeability, which reads as

$$k_{int} = k_{int,undamaged} + k_{int,damaged} \tag{14}$$

where $k_{int,undamaged}$ is approximated as a function of the total porosity of the rock

$$k_{int,undamaged} = k_{int,0} e^{A\left(\frac{\varphi}{\varphi_0}-1\right)} \tag{15}$$

and $k_{int,damaged}$ introduces the damage induced increase in permeability

$$k_{int,damaged} = \frac{D}{D_{kmax}}\left(k_{max} - k_{int,undamaged}\right) \tag{16}$$

where $k_{int,0}$ (m^2) is the initial intrinsic permeability, φ_0 (−) is the initial porosity, A (−) is an empirical factor calibrated from the experimental tests, k_{max} (m^2) is the experimental maximum permeability of the damaged sedimentary rock and D_{kmax} (−) is the experimental rock damage value that corresponds to k_{max}.

KAERI-D uses TOUGH2-FLAC3D to simulate the one-dimensional test and COMSOL Multiphysics® for the three-dimensional test. Different discretisation methods have been used: (i) a three-dimensional finite difference grid has been used for experiment 1 and (ii) a three-dimensional finite element mesh for experiment 2, see Appendix A.2.

The NCU/TPC-V model is another continuous multiphase hydro-mechanical model, whose development is based on the theory of Suk and Yeh[35,36] and Tsai and Yeh.[37,38] In this model, the mechanical theory proposed by Liu[39,40] and Liu et al.[41] is used and applied to visco-elastic materials.[42] The k-S-P model presented by Parker et al.[43] is used to describe the relationships between relative permeability, fluid saturation and pressure within each phase.

Mass conservation equation for each fluid phase (assuming L phases) is given by

$$\frac{\partial \rho_\alpha \varphi S_\alpha}{\partial t} + \nabla\cdot(\rho_\alpha \mathbf{v}_\alpha) + \nabla\cdot(\rho_\alpha \varphi S_\alpha \mathbf{v}_s) = M^\alpha\ ,\ \alpha\in\{L\}\quad \sum_{\alpha=1}^{L} S_\alpha = 1 \tag{17}$$

whereas for the solid phase is

$$\frac{\partial \rho_s \varphi_s}{\partial t} + \nabla\cdot(\rho_s \varphi_s \mathbf{v}_s) = 0 \tag{18}$$

where $\rho_{\alpha/s}$ (kg/m^3) is the density of the α-th fluid/solid phase, S_α (−) is the normalized saturation of theα-th fluid phase, $\mathbf{v}_{\alpha/s}$ (m/s) is the Darcy velocity of the α-th fluid/solid phase (with $\mathbf{v}_s = \frac{d\mathbf{u}}{dt}$, $\mathbf{u}$ the displacement of the media), φ_s (−) is the volume fraction of the solid phase ($\varphi = 1 - \varphi_s$), and M^α ($kg{\cdot}m^{-3}{\cdot}s^{-1}$) is the sum of the artificial source/sink rates of all species in theα-th fluid phase.

The momentum equation under approximately equilibrium state is represented by

$$-\nabla\cdot\mathbf{T} + \sum_{\alpha\in\{L\}}\nabla(S_\alpha p_\alpha) - \left[\sum_{\alpha\in\{L\}}\rho_\alpha\varphi S_\alpha + \rho_s\varphi_s\right]\mathbf{g}\nabla\mathbf{z} = -\varphi_s\rho_s\frac{d^2\mathbf{u}}{dt^2} \approx 0 \tag{19}$$

where p_α (Pa) is the pressure of the α-th fluid phase, $\mathbf{T}$ (Pa) is the Cauchy stress tensor, $\mathbf{g}$ is the gravitational acceleration (m/s^2) and $\mathbf{z}$ (m) is the potential head.

In this model, the solid-phase pressure p_s (Pa) reads as

$$p_s = p_{s0} - \frac{1}{\alpha} ln\left(\frac{1-\varphi_s}{1-\varphi_{s0}}\right) \tag{20}$$

where p_{s0} (Pa) is the referenced pressure of the solid phase, φ_s (−) is the volume fraction of the solid phase, φ_{s0} (−) is the referenced volume fraction of the solid phase and α (−) is the parameters of the constitutive law. Here, the intrinsic permeability tensor $\mathbf{k}_{int}$ (m^2) depends on the pore size as follows

$$\mathbf{k}_{int} = \mathbf{k}_{int,0}\left(\frac{1}{1+(\varphi_0-\varphi)}\right)^n \tag{21}$$

where $\mathbf{k}_{int,0}$ (m^2) is the reference intrinsic permeability, φ_0 (−) is the reference porosity, φ is the porosity and n (−) is the fractional exponent depending on the particle size and packing structure.

This two-phase flow model is coupled to a non-linear visco-elastic model. Indeed, the effective stress tensor can be written as

$$\sigma' = C : \left[\nabla\mathbf{u} + (\nabla\mathbf{u})^T\right] \tag{22}$$

where C is a function of the high-order term $(\nabla\mathbf{u})^2$, the gradient of the displacement rate $\nabla\dot{\mathbf{u}}$, the compressibility of the media, the Young's modulus and the Poisson's ratio.

NCU/TPC-V uses a three-dimensional in-house thermo-hydro-mechanical-chemical software to numerically simulate both experiments, see Appendix A.2 for more numerical details.

Note that other preliminary continuous models have been developed during the task, see Tamayo-Mas et al.[18],[19] for a brief description. In these numerical models, standard two-phase flow equations were coupled to a rigid porous medium (model UPC/Andra-H), with linear elasticity (models LBNL-C, CNSC-E) and with a damage model (model CNSC-D). However, due to their difficulty in reflecting the underlying physics of gas migration fluxes in a 1D experiment (experiment 1), they were not applied to a 3D test (experiment 2) and are not reported in this paper.

3.2. Enhanced two-phase flow models

Two different enhanced two-phase flow models (UPC/Andra-ED and LBNL-D) have been developed. In these approaches, fractures are considered to behave as preferential pathways. In model UPC/Andra-ED, fractures are not explicitly represented but embedded within a plastic material whereas model LBNL-D is a lattice approach that allows the discrete representation of fracture formations during coupled THM processes. During the task, and as reviewed by Tamayo-Mas et al.[18],[19]; other approaches where embedded fractures are coupled to an elastic medium (models UPC/Andra-HM1 and UPC/Andra-HM2) have also been developed but finally dismissed, since elasticity was not considered to be the appropriate mechanical behaviour, and thus, not included in this paper.

Model UPC-Andra-ED is a heterogeneous continuous two-phase model, where the standard equations of balance of water, balance of gas and equilibrium of stresses are solved. This approach is characterised by the coupling of these standard equations to embedded fractures,[44] which allow the representation of preferential paths. Hence, the global intrinsic permeability is defined as a function of material matrix (Eq. (26)) and internal fracture permeabilities (Eq. (27)) and reads

$$k_{int} = k_{matrix} + k_{fractures} \tag{23}$$

whereas liquid- and gas-phase permeabilities read

$$k_{liquid} = \left(S_{eff,\ liquid}\right)^{n_{liquid}}\left(k_{matrix} + k_{fractures}\right) \tag{24}$$

$$k_{gas} = \left(S_{eff,\ gas}\right)^{n_{gas}^{matrix}} k_{matrix} + \left(S_{eff,\ gas}\right)^{n_{gas}^{fractures}} k_{fractures} \tag{25}$$

respectively, with $S_{eff,\ liquid/gas}$ (−) being the saturation degree for liquid or gas and $n_{liquid/gas}^{matrix/fractures}$ (−) a power-law exponent for each case state (i.e. for liquid or gas state, and for matrix or fractures media).

The matrix permeability component is calculated as

$$k_{matrix} = \frac{k_0(1-\varphi_0)^2}{\varphi_0^3}\frac{\varphi^3}{(1-\varphi)^2} \tag{26}$$

where k_0 (m^2) is the initial permeability (randomly distributed along the material), φ_0 (=0.44) is the initial porosity and φ (−) is the actual porosity value, changing in space and time during the test. The permeability is also controlled by the internal fractures with

$$k_{fractures} = \frac{b^3}{12a} \tag{27}$$

where a (m) refers to the associated width for each fracture (which is equivalent to the assumed spacing between fractures) and b (m) is the aperture of the fractures. This value depends on the strain ε (−) and on the initial strain ε_0 (−) and may be computed as

$$b = b_0 + \varepsilon - \varepsilon_0 a \leq b_{max} \tag{28}$$

with b_0 (m) and b_{max} (m) being the initial and maximum aperture of the fractures.

As stated in Eqs. (24) and (25), liquid and gas relative permeabilities are defined by the effective saturation degree of liquid and gas respectively. Hence,

$$k_{r,liquid/g} = \left(S_{eff,\ liquid/gas}\right)^{n_{liquid/gas}} = \left(\frac{S_{liquid/gas} - S^{min}_{liquid/gas}}{S^{max}_{liquid/gas} - S^{min}_{liquid/gas}}\right)^{n_{liquid/gas}} \tag{29}$$

The retention curve may change with the opening of fractures as pore size controls gas entry values, and fractures may play the role of big pores leading to a reduction of gas entry value. The capillary pressure can then be calculated as

$$p_c = p_0 \sqrt[3]{\frac{k_0}{k}} \tag{30}$$

UPC/Andra implemented their model using the Code_bright code, see Appendix A.2 for details.

A second enhanced model (LBNL-D) was developed by LBNL. This model is a discontinuous two-phase flow model with mechanical deformation and fracture/damage processes. The Rigid-Body-Spring Network (RBSN), a lattice approach, is linked to the flow simulator (TOUGH2) in order to facilitate a discrete representation of fracture formations. Indeed, two types of elements are used for the numerical simulations: (i) cell and (ii) interface elements. Cell-type elements represent the matrix/grain bulk, for which the porosity-dependent permeability is defined as in model UPC/Andra-ED (see Equation (26)). Interface-type elements represent potential fractures or pre-existing fractures embedded in a portion of matrix volume. As done by UPC/Andra, the permeability is calculated as the sum of two components (see Equation (23)), where each component is conditionally calculated based on the fracture activation. Hence, if an interface element is yet to be fractured, k_{matrix} is calculated as in cell-type elements and $k_{fractures}$ is simply assumed to be zero. On the other hand, if the interface element is fractured, $k_{fractures}$ tends to dominate, enhancing the total permeability and k_{matrix} is assumed to revert to the initial intrinsic permeability $k_{int,0}$. That is,

$$k = \begin{cases} \dfrac{k_0(1-\varphi_0)^2}{\varphi_0^3}\dfrac{\varphi^3}{(1-\varphi)^2}, & \textit{if unfractured} \\ k_0 + \dfrac{b^3}{12a}, & \textit{if fractured} \end{cases} \tag{31}$$

where a (m) is the element width and b (m) is the aperture.

LBNL-D uses a van Genuchten capillary pressure model and thus, the water retention curve is defined as

$$p_c(S) = p_0^{'}\left(\left(S^*\right)^{-\frac{1}{\lambda}} - 1\right)^{1-\lambda} \tag{32}$$

where λ (−) is the van Genuchten parameter, $S^* = \frac{S_l - S_{lr}}{1 - S_{lr}}$, with S_l (−) being the liquid saturation and S_{lr} (−) being the residual liquid saturation. The relevant capillary pressure parameters of cell-type elements are adopted from the specifications of Senger and Marschall[45] whereas for fracture elements,

$$p_0^{'} = p_0 \sqrt[3]{\frac{k_0}{k}} \tag{33}$$

A Corey relative permeability model[46] is used to define the permeability-saturation relationships of both liquid

$$k_{r,l}(S) = \widehat{S}^4 \tag{34}$$

and gaseous phases

$$k_{r,g}(S) = m_g\left(1 - \widehat{S}\right)^2\left(1 - \widehat{S}^2\right) \tag{35}$$

where $\widehat{S} = \frac{S - S_{lr}}{1 - S_{lr} - S_{gr}}$ and m_g is a multiplying factor for the enhanced gas permeability. The residual saturations $S_{lr}$and S_{gr} are provided to limit the mobility of the respective phase, i.e., both liquid and gaseous phases can vary their mobilities only in the range of $S = [S_{lr}, 1 - S_{gr}]$. To avoid unphysical situations with $p_c = \infty$, larger S_{lr} for the relative permeability is usually chosen as compared to S_{lr} for the capillary pressure.[47]

Pressure and flow responses observed from the gas injection experiments suggest that gas only flows into the fully saturated specimen at a certain level of gas pressure or above. This conditional gas penetration is implemented by introducing a gas entry pressure with the corresponding residual gas saturation (S_{gr}) in the capillary pressure function.

In experiment 1, and as done in other models (see for instance model BGR/UFZ-E), effective (grain-to-grain) stress σ' is calculated from the pore pressure p based on the linear poro-elasticity theory[48] and hence,

$$\sigma' = \sigma - \alpha p \tag{36}$$

where σ (Pa) is the total normal stress obtained from overall loading and $p = \max(p_g, p_l)$ (Pa) is taken as the maximum pressure between gas and liquid phases. In experiment 2, in order to obtain better stress results, the effective stress is defined by using a more general formulation. Indeed, the effective stress is thus defined as

$$\sigma' = \sigma - p_g + \chi\left(p_g - p_l\right) \tag{37}$$

where χ (−) is the Bishop's coefficient already introduced in CNSC-PD defined as

$$\chi = \begin{cases} 1, & \textit{if } p_g - p_l < p_g^{entry} \\ \left(\dfrac{p_g - p_l}{p_g^{entry}}\right)^{-0.55}, & \textit{if } p_g - p_l \geq p_g^{entry} \end{cases} \tag{38}$$

where p_g^{entry} (Pa) is a gas entry pressure.

LBNL-D model takes into account the shrinkage/swelling effect due to the local changes of liquid saturations and hence,

$$\Delta\varepsilon_s = \alpha_s \Delta S \tag{39}$$

where ε_s (−) is the shrinkage/swelling strain and α_s (−) is the hydraulic shrinkage coefficient.

In this approach, fractures are modelled by the degradation of the rigid-body springs. Indeed, a fracture event involves a reduction of the spring stiffness and a release of the associated element forces. The reduction of the stiffness is accounted for by the introduction of a damage parameter,

$$\mathbf{D}' = (1 - D)\mathbf{D} \tag{40}$$

where D (−) is a scalar damage index that directly switches from 0 (undamaged) to 1 (completely damaged) once a fracture event occurs (i.e., when the stress state of an element violates the failure criteria). Here, the Mohr-Coulomb criterion has been used to determine the failure of lattice elements.

3.2.1. Single-phase flow models

Quintessa/RWM developed a fully-coupled single-phase hydro-mechanical model to simulate both experiments. Their approach in developing this model has been to focus on methods that can be used in

upscaled applications and therefore have been primarily interested in reproducing key deterministic features from the experiments considered within the Task in a coarsely discretised model. In this model, gas transport through the system is modelled using Richards' equation (which can be applied since gas flow is very fast compared to water flow), which is used to solve

$$\frac{\partial}{\partial t}\left(\theta_g \rho_g\right) = -\nabla\cdot\left(\rho_g \mathbf{q}_g\right) \tag{41}$$

where ρ_g (kg m^{-3}) is the density of the fluid, θ_g (−) is the volume fraction of the fluid within the medium, and $\mathbf{q}_g$ (m s^{-1}) is the Darcy flux vector. From Darcy's law $\mathbf{q}_g$ is defined as

$$\mathbf{q}_g = -\frac{k_g}{\mu_g}\left(\nabla p_g + \rho_g g \nabla z\right) \tag{42}$$

where k_g (m^2) is the intrinsic permeability of the medium for the fluid, μ_g (Pa s) is the dynamic viscosity of the fluid, p_g (Pa) is the pressure of the fluid, g (m s^{-2}) is the acceleration due to gravity and z (m) is the vertical height coordinate. Note that, in practice, the gradient contribution due to changes in vertical z-coordinate is omitted for the horizontal 2D axisymmetric cylindrical geometry used to model the Task A experiments.

The choice of a single-phase fluid model is based on gas injection experiments through saturated bentonite,[49,10,50] where there is minimal water displacement throughout the duration of the experiment, and no significant movement of water when considered as a separate phase in earlier models.[51,18,19]

Gas permeability evolution in the model is captured by processes representing capillary opening/closing, whereby flow is considered through capillary tubes with the opening of capillaries dependent on the degree by which the gas pressure exceeds the total stress of the system, and micro-scale deformation (creep). These processes are represented in the model through the permeability of the gas, k_g (m^2), and the volume fraction of gas, θ_g (−). Hence,

$$k_g = k_{cap} + k_{creep} \tag{43}$$

$$\theta_g = \theta_{cap} + \theta_{creep} \tag{44}$$

where the parameters k_{cap} (m^2), θ_{cap} (−), k_{creep} (m^2) and θ_{creep} (−) are the calculated permeability and volume fraction components associated with the capillary opening/closing process and micro-scale deformation process, respectively. Quintessa/RWM-ECap approach assumes a Hagen-Poiseuille pipe flow model (see Bond et al.[16]) with cylindrical capillaries and thus,

$$k_{cap} = \frac{\pi r^4}{8 a_c} \tag{45}$$

and

$$\theta_{cap} = \frac{\pi r^2}{a_c} \tag{46}$$

where a_c (m^2) is the capillary spacing (inverse of the capillary density) and r (m) is the capillary radius, which is coupled to the stress of the system using the linear elastic relationship

$$r = r_0 + \frac{\gamma}{r_0}\left(\varepsilon_c\left(p_g, \sigma_{tot}\right) - \varepsilon_{c0}\right) \tag{47}$$

where r_0 (m) is the reference capillary radius associated with the reference stress for capillary opening, ε_{c0} (Pa), ε_c (Pa) is the stress acting to open the capillary, which is a function of how the gas pressure exceeds the total stress, σ_{tot} (Pa), and γ (m^2 Pa^{-1}) is the capillary compressibility.

Different forms may be used to describe ε_c. Indeed, in experiment 1,

$$\varepsilon_c = p_g - \sigma_{tot} \tag{48}$$

and in experiment 2,

$$\varepsilon_c = p_g - (1 - D)\sigma_{tot} \tag{49}$$

where D (−) is a damage term that captures the decrease in injection pressure observed in the experiment after the breakthrough. This damage term is defined by

$$D_0 = 0$$

$$\frac{dD}{dt} = \begin{cases} D_{acc}, & p_g > (1-\delta)\sigma_{tot} \text{ and } D < D_{max} \\ 0, & otherwise \end{cases} \tag{50}$$

where D_{acc} (s^{-1}) is the rate of damage accumulation and D_{max} (−) is the maximum amount of damage.

The micro-scale deformation process is described by

$$\theta_{creep,0} = \theta_{creep,ref}$$

$$\frac{d\theta_{creep}}{dt} = \begin{cases} c_r \theta_{creep} \dfrac{p_g - p_{creep}}{p_{creep}}, & p_g > p_{creep} \text{ and } \theta_{creep} \le \theta_{creep}^{max} \\ 0, & otherwise \end{cases} \tag{51}$$

$$k_{creep} = a_{creep}\left(\theta_{creep} - \theta_{creep,ref}\right) \tag{52}$$

where $\theta_{creep,ref}$ (−) is the reference initial dilated gas porosity associated with micro-scale deformation, c_r (s^{-1}) is a creep rate constant, p_{creep} (Pa) is the threshold pressure for creep, θ_{creep}^{max} (−) is the creep limit and a_{creep} (m^2) is the creep permeability constant.

This single-phase flow approach is coupled to a mechanical model, where the standard Cauchy momentum balance equation is solved. The mechanical coupling uses the calculated total stress for the above-mentioned hydro-model and an effective stress formulation relating the pore pressure, p (Pa), to the gas pressure via the Biot coefficient α (−):

$$p = \alpha p_g \tag{53}$$

Quintessa/RWM-ECap model includes an injection system to ensure that it is self-consistent in terms of the gas injection pressure boundary condition. In order to calculate it, the injector is explicitly modelled using the ideal gas law using pump flow rates/gas refills from the relevant experiment dataset.

This model is a combination of two previously presented modelling approaches: (1) a fully-coupled two-phase Darcy flow capillary-opening model with separate permeabilities for gas and water (see Tamayo-Mas et al.[18,19]) and (2) a simple empirical model used to capture the key deterministic behaviours of the experiments using Richards' equation with the localised micro-scale deformation process used to generate pathways dynamically described by Bond et al.[51] Further details of this model and other intermediate investigations and numerical models can be found within Bond et al.[51,52].

3.3. Conceptual chaotic model

Experimental data show that gas migration in a water-saturated compacted clay material exhibits rich nonlinear dynamic behaviours as the injection gas pressure varies: from a constant flow to a periodic flow and eventually to a chaotic behaviour, see Wang et al.[53] To capture these nonlinear behaviours, SNL developed another model, where special emphasis was placed on the capture of dilatancy. This is based on the concept of the delay logistic model[54,55] and its underlying assumption that given the low permeability of the material, the dominant mechanism for gas migration is first to form a bubble nucleation and then to push the bubble through the clay matrix through matrix dilation

and fracturing. Thus, the evolution of mass and pressure within a bubble of a volume V is simply expressed by

$$\frac{dM}{dt} = k_u(p_u - p) - k_d(p - p_d) \tag{54}$$

where M is the gas mass in the bubble; p is the gas pressure in the bubble; p_u and p_d are the gas pressures in the upstream and the downstream of the bubble movement respectively; k_u and k_d are the permeability of the matrix in the upstream and the downstream of the bubble movement respectively; and t is the time.

For the sake of simplicity, k_u and k_d are assumed to be proportional to the gas pressure p. Thus,

$$k_u = k_u^0 p \tag{55}$$

$$k_d = k_d^0 p \tag{56}$$

where k_u^0 and k_d^0 are constant. Then, and assuming the ideal gas law, Eq. (54) becomes the continuous logistic equation

$$\frac{dp}{dt} = \lambda_1 p\left(1 - \frac{p}{K}\right) \tag{57}$$

with

$$\lambda_1 := \frac{(k_u^0 p_u + k_d^0 p_d)RT}{V} \tag{58}$$

$$K := \frac{\lambda_1}{\lambda_2} \tag{59}$$

$$\lambda_2 := \frac{(k_u^0 + k_d^0)RT}{V} \tag{60}$$

In order to account for the clay "memory" effect, the permeabilities k_u and k_d are assumed to depend not only on the current pressure value (see Eqs. (55) and (56)) but on the pressure history. Thus, Eq. (57) becomes

$$\frac{dp}{dt} = \lambda_1\left(1 - \frac{p}{K}\right)\int_{-\infty}^{t} G(t-s)\bar{p}(s)ds \tag{61}$$

where $G(t)$ is a kernel function characterising the influence of the pressure at a previous step on the permeability at the current time step. A commonly chosen kernel function is an exponential function characterising an exponential decay of the influence as the time interval increases:

$$\frac{dp}{dt} = \lambda_1\left(1 - \frac{p}{K}\right)\int_{-\infty}^{t} \alpha e^{-\alpha(t-s)}\bar{p}(s)ds \tag{62}$$

For an illustration of the concept of bifurcation and chaos for gas migration, let's assume the gas movement is more or less stepwise. Equation (57) can then be reduced to a logistic map

$$p_{n+1} = \lambda p_n(1 - p_n) \tag{63}$$

with

$$\lambda = 1 + \lambda_1 \Delta t \tag{64}$$

It is known that Equation (63) can exhibit rich dynamic behaviours.[55]

To test if the flow rate variation is truly chaotic, a time series analysis was performed for gas inflow and outflow measurements obtained from bentonite Mx80-D (Fig. 8). The time series was first divided into four segments based on the time variation of injection pressure. The calculations were performed to evaluate the embedded dimension using the false nearest neighbour method for each segment. By means of this

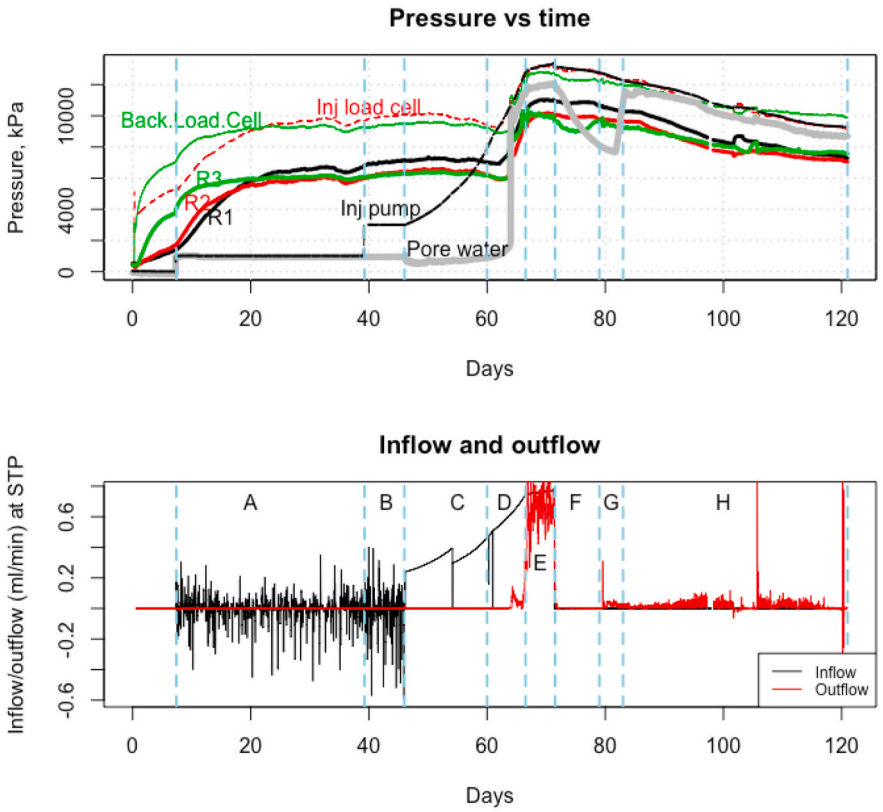

Fig. 8. Gas inflow and outflow time series obtained from bentonite Mx80-D and segmentation of the data for time series analysis. Segments A and B are for inflow and segments E and H are for outflow.

algorithm, it is found the embedded dimension for the gas migration phenomenon ranges from 3 to 4 (Fig. 9). It is shown that in the embedded space the flow rate seems to possess an internal structure (a chaotic attractor), i.e., not completely random (white noise), indicating a deterministic chaotic behaviour which can be described by 3–4 independent variables. This is further confirmed by the calculation of the spectrum of Lyapunov exponents for gas inflow. A Lyapunov exponent of a dynamical system characterises the rate of separation of infinitesimally close trajectories. A positive maximal Lyapunov exponent is usually an indication of a chaotic behaviour of the system. As shown in Fig. 10, gas migration in a water-saturated compacted bentonite system is a deterministic chaotic process.

Due to the preliminary nature of this chaotic model, this is not taken into account in the comparison analysis of Section 4.

4. Results

Experimental data can be summarised by four key components: (i) a quiescence phase, followed by (ii) the gas breakthrough, which leads to a (iii) peak value, which is then followed by (iv) a negative decay, see Fig. 11. Thus, models have been assessed by these different aspects.

Radial stress results for experiment 1 (1D gas flow) and experiment 2 (spherical (3D) gas flow) are shown in Fig. 12 and Fig. 13 respectively. As seen, due to the chaotic behaviour of gas flow, evolution of stress has not been compared at particular locations but against the whole range of stresses. A visual inspection of the data indicates that:

- **Quiescence phase**: some models obtain good initial values while others under-predict them (BGR/UFZ-E and CNSC-PD in experiment 1; BGR/UFZ-E, KAERI-D and UPC/Andra-ED in experiment 2).
- **Gas breakthrough**: in experiment 1, the form of the breakthrough is reasonably well captured but teams struggle with some of the specifics such as the breakthrough pressure or the timing. Indeed, modelled radial stresses at gas breakthrough time (within a window of ± 4 days) substantially differ from the physically-observed values (differences beyond 1 MPa are obtained) and simulated curves show precursor events which are not reflected in the data. Models do not capture the complexity of experiment 2, where at least three short-lived breakthrough events can be observed before a sustained breakthrough is achieved (see Fig. 6), though given the focus of most teams on representing behaviours that would be expected to be reproducible between experiments, this is not surprising. Indeed, most models only predict a single breakthrough event. Hence, comparing the numerical predictions with the experimental results fairly is difficult since it is not obvious which of the experimental breakthroughs are best for the comparison. Some of the models exhibit a breakthrough that appears consistent with the experiment (BGR/UFZ-E, KAERI-D, NCU/TPC-V, LBNL-D, Quintessa/RWM-ECap) whereas some others do not have a discernible breakthrough event. That said, such models still have value in guiding both phenomenological understanding and future model development depending on their intended end-use.
- **Peak values**: in experiment 1, they are correctly captured by some models (BGR/UFZ-E, CNSC-PD, Quintessa/RWM-ECap and UPC/Andra-ED) while they are over-estimated in other cases (KAERI-D, LBNL-D and NCU/TPC-V). In experiment 2, peak values are not correctly captured in general and only in some models (KAERI-D, NCU/TPC-V and Quintessa/RWM-ECap) are they reasonably well described.
- **Negative decay**: most of the models are capable of obtaining a good fitting with respect to the experimentally-observed negative decay in both experiments.

Similar results are obtained in terms of the axial stress in experiment 1, see Fig. 14. In experiment 2, see Fig. 15, due to the increased variance in data (due to localisation of gas flow), better fittings are in general obtained. However, when up-scaling, the representation of localisation will need to be addressed.

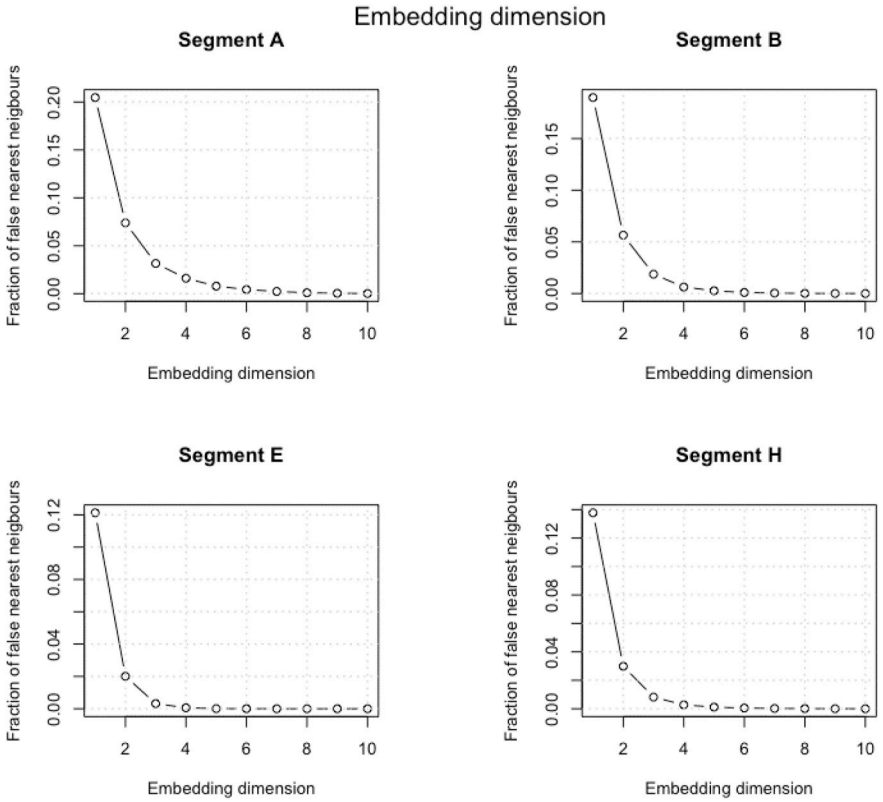

Fig. 9. Global Embedding Dimensions calculated for Segments A, B, E and H.

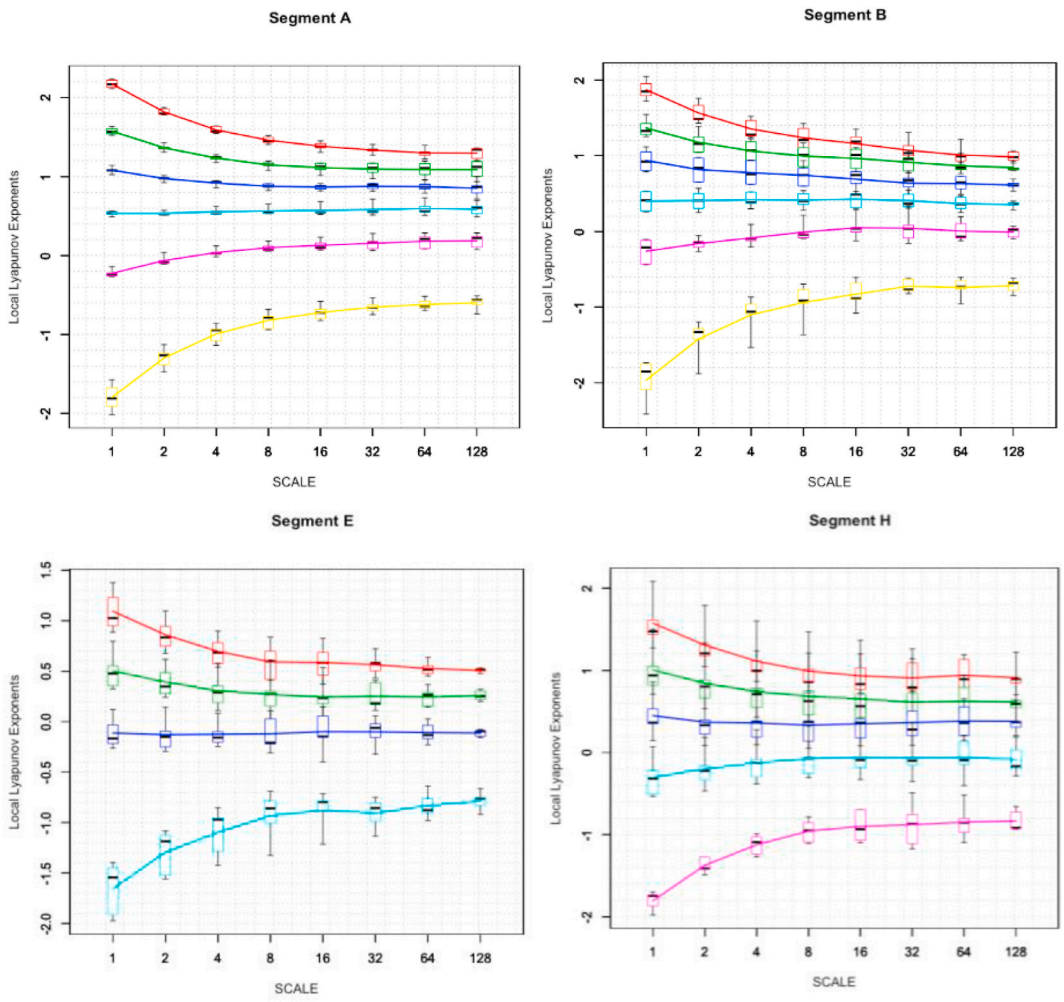

Fig. 10. Spectrum of Lyapunov exponents calculated for segments A, B, E and H. The sum of positive and negative Lyapunov exponents is positive, indicating that the attractors are not converging, likely due to the presence of a stochastic component.[55]

In experiment 1, pore pressure evolutions have also been compared against experimental data, see Fig. 16. Similarly as with stresses, a visual inspection of the pore pressure data indicates that:

- **Quiescence phase**: most of the teams obtain good initial values.
- **Gas breakthrough**: this remains a difficult experimental feature to capture. Indeed, although the rapid increase in pore pressure is modelled by all the teams, for some models (BGR/UFZ-E, KAERI-D, UPC/Andra-ED, Quintessa/RWM-ECap) this is obtained at earlier times and more gradually than seen in the experiment. This may be explained by a numerical diffusion effect which is necessary to get gas into the sample.
- **Peak values**: reasonably good peak values are obtained with most of the models and only some of them (BGR/UFZ-E and CNSC-PD) lead to under-predicted values.
- **Negative decay**: the post-peak shape trend is well defined by all models.

Note that the reported pore pressures may include either gas and water components or only a gas component depending on the approach taken by the individual teams.

Varying results are also observed in the prediction of the outflow curves. As seen in Fig. 17a, most of the models are able to capture the rapid increase in flow detected in experiment 1. However, simulated curves generally show precursor events which are not reflected in the experimental data. The observed shape of the post-breakthrough curve is poorly reflected by all the models except for Quintessa/RWM-ECap, that uses a 'capillary' compressibility term to fit the opening and closing of pathways from gas testing. In experiment 2, see Fig. 17c, some models (KAERI-D, LBNL-D, Quintessa/RWM-ECap and UPC/Andra-ED) are able to capture the rapid increase in flow (although some precursor events are also obtained) and the shape of the post-breakthrough curve. In experiment 2, these profiles have been directly compared with modelled inflows (see Fig. 17b).

5. Discussion

Eight different numerical models have been developed to simulate both experiment 1 (1D gas flow) and experiment 2 (spherical (3D) gas flow). As observed in section 4, a great effort from the modelling teams has been made to tackle these two experiments and clear progress has been made by extending existing approaches to 2D and 3D that are now able to match key aspects of the evolution (peak values, flow, pressure, decay …). Indeed, all models are able to represent a number of physical characteristics of the two experiments. However, none of the models describe the full complexity of the physical processes observed in these experiments.

Several aspects play an essential role when it comes to assessing and comparing the numerical models. As seen in Appendix A.1 and Appendix A.2 respectively, different codes and different test geometries have been used by the teams which makes it difficult to compare results and parameterisations directly across the teams. Initial and boundary

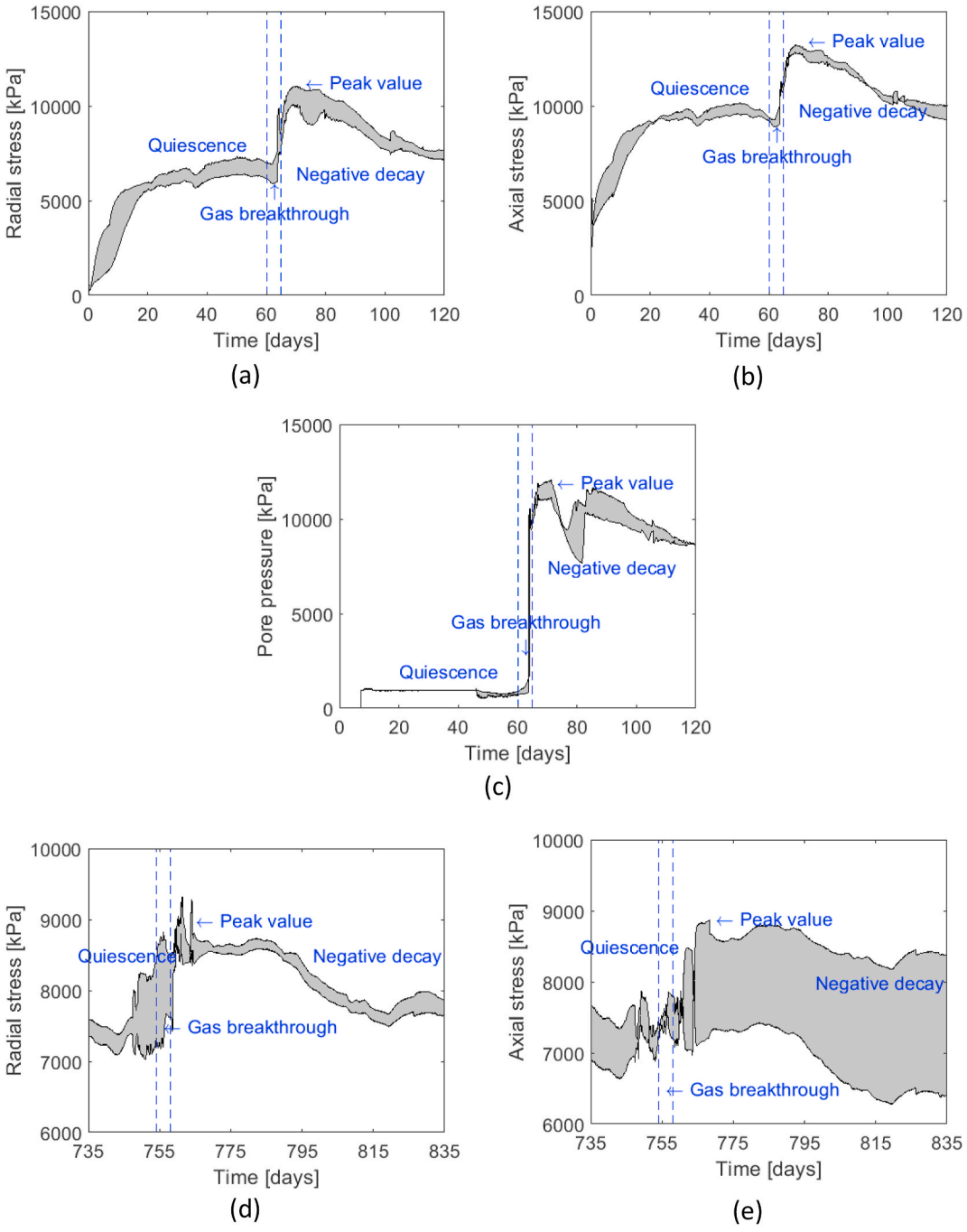

Fig. 11. Key components that characterise experiment 1 ((a) radial stresses, (b) axial stresses, (c) pore pressures) and experiment 2 ((d) radial stresses (e) axial stresses), see sections 2.1 and 2.2 respectively.

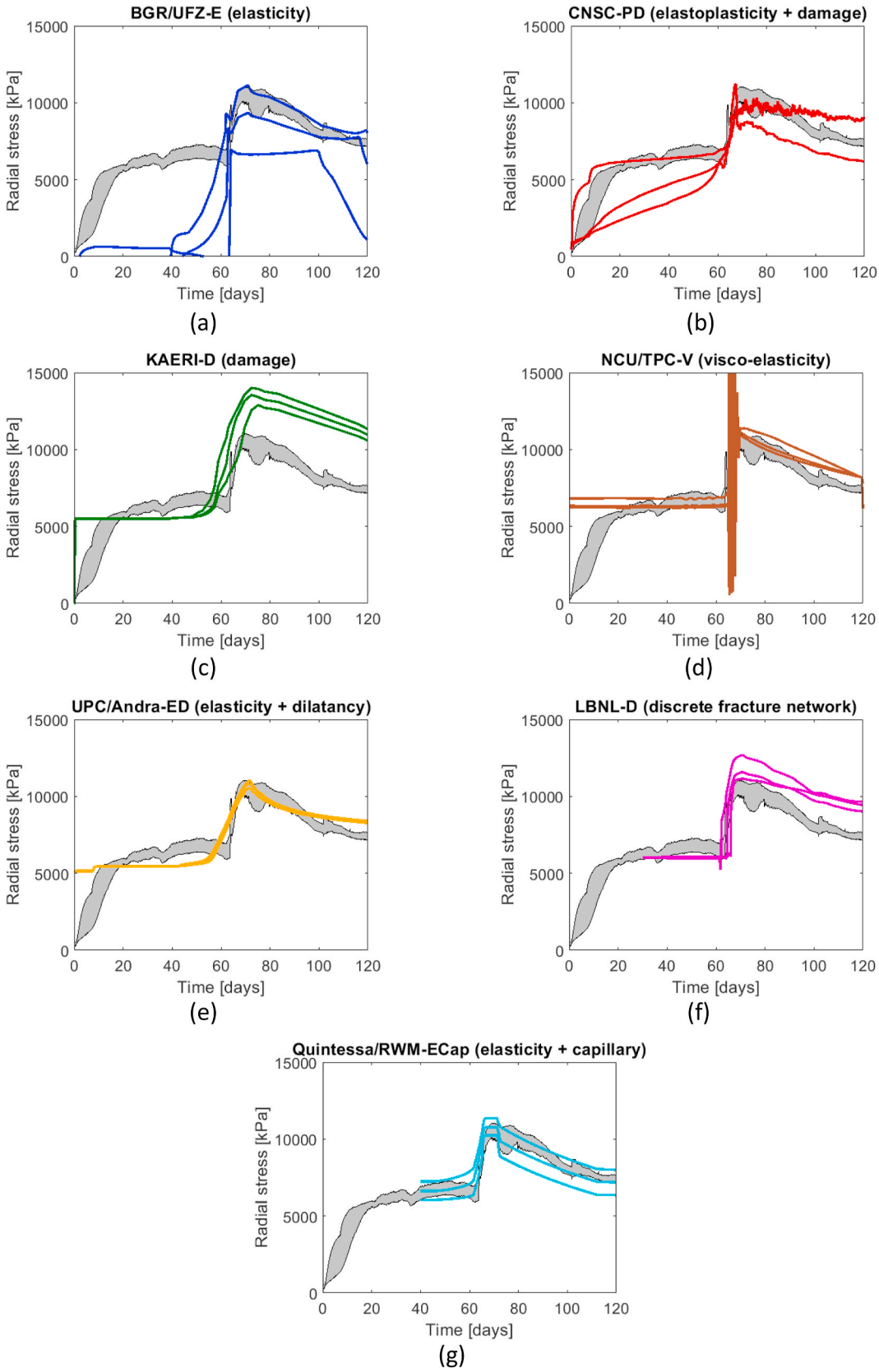

Fig. 12. Experiment 1: experimental versus numerical radial stresses, obtained with models (a) BGR/UFZ-E, (b) CNSC-PD, (c) KAERI-D, (d) NCU/TPC-V, (e) UPC/Andra-ED, (f) LBNL-D and (g) Quintessa/RWM-ECap.

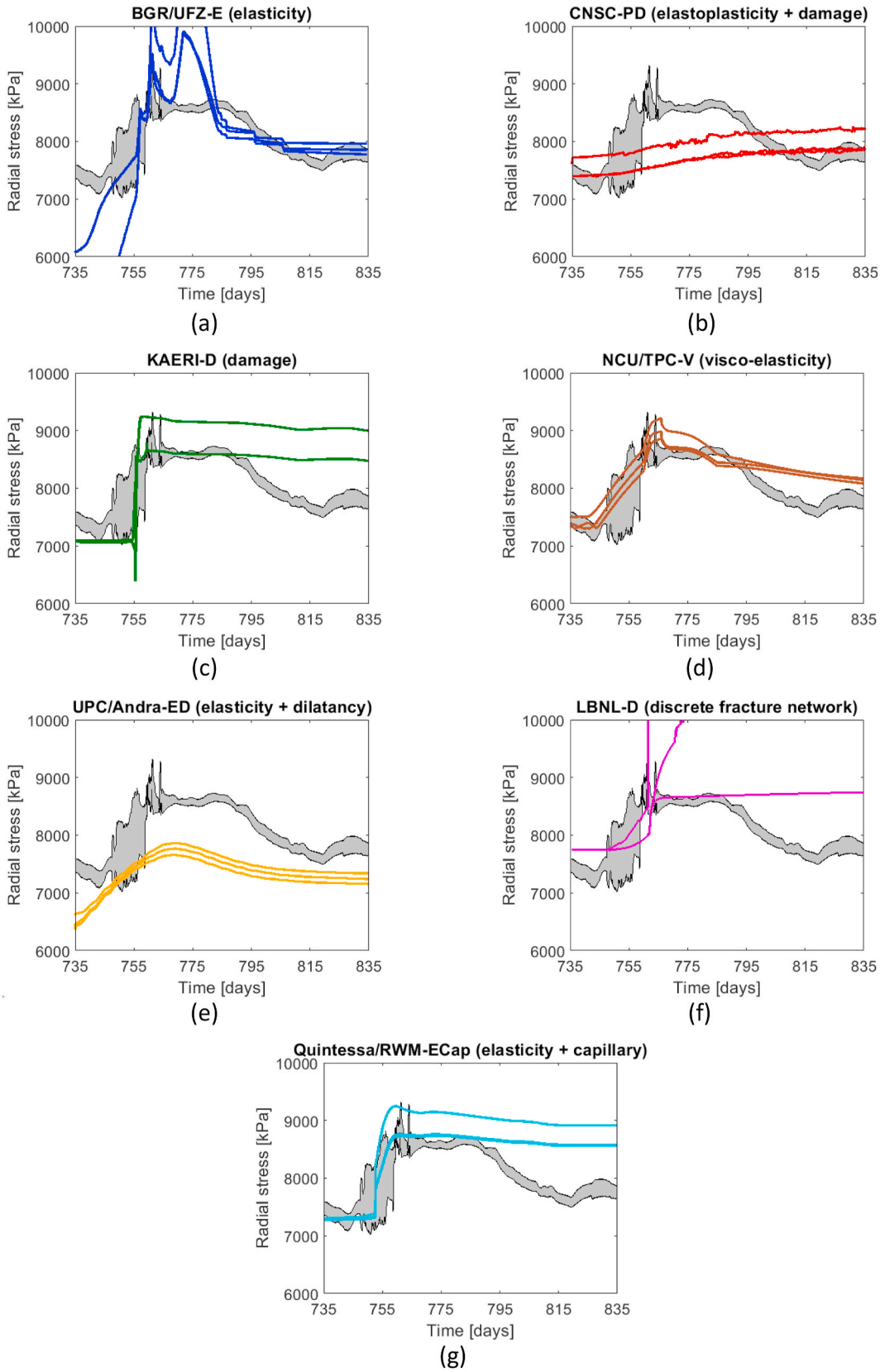

Fig. 13. Experiment 2: experimental versus numerical radial stresses, obtained with models (a) BGR/UFZ-E, (b) CNSC-PD, (c) KAERI-D, (d) NCU/TPC-V, (e) UPC/Andra-ED, (f) LBNL-D and (g) Quintessa/RWM-ECap.

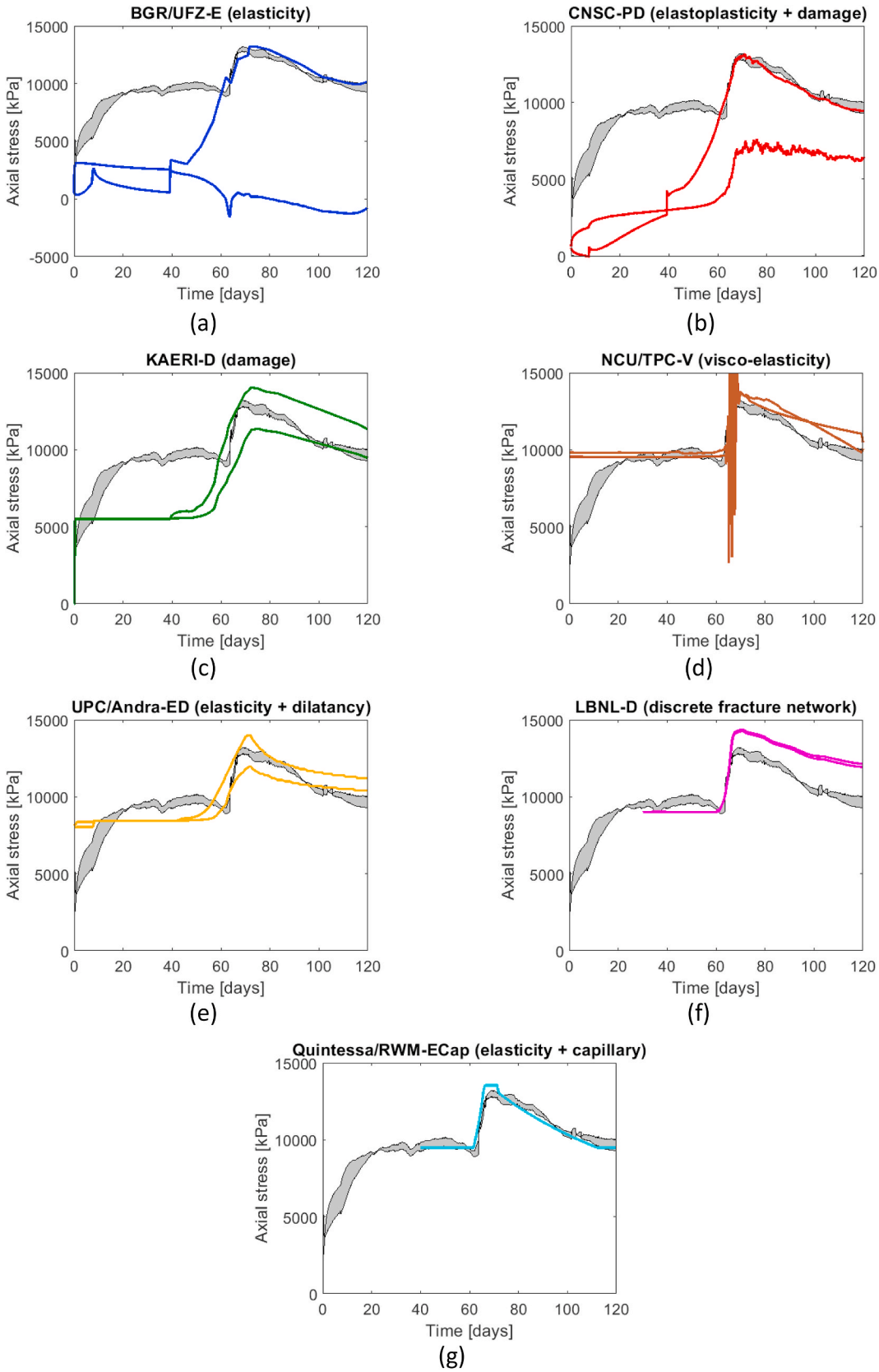

Fig. 14. Experiment 1: experimental versus numerical axial stresses, obtained with models (a) BGR/UFZ-E, (b) CNSC-PD, (c) KAERI-D, (d) NCU/TPC-V, (e) UPC/Andra-ED, (f) LBNL-D and (g) Quintessa/RWM-ECap.

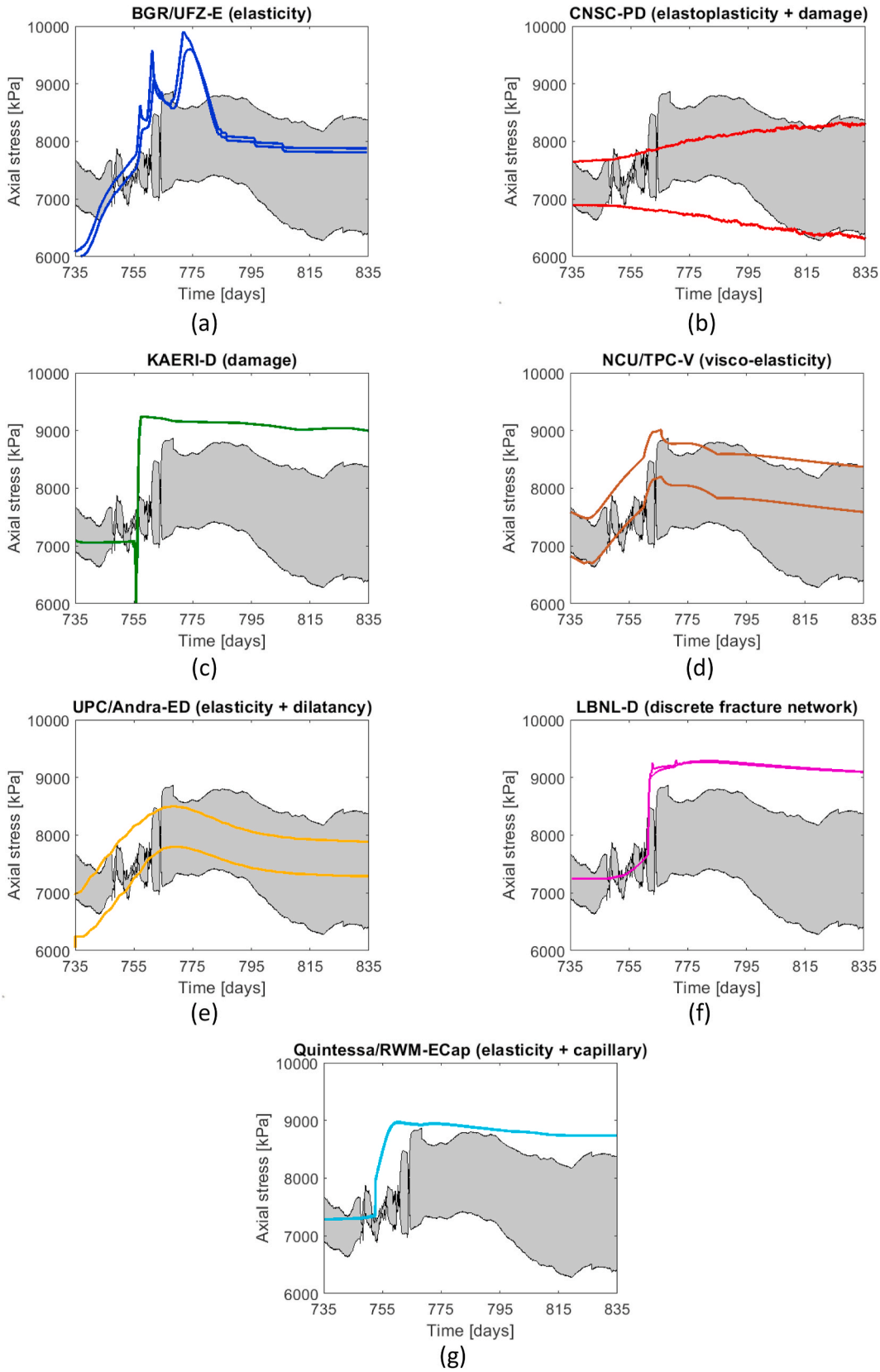

Fig. 15. Experiment 2: experimental versus numerical axial stresses, obtained with models (a) BGR/UFZ-E, (b) CNSC-PD, (c) KAERI-D, (d) NCU/TPC-V, (e) UPC/Andra-ED, (f) LBNL-D and (g) Quintessa/RWM-ECap.

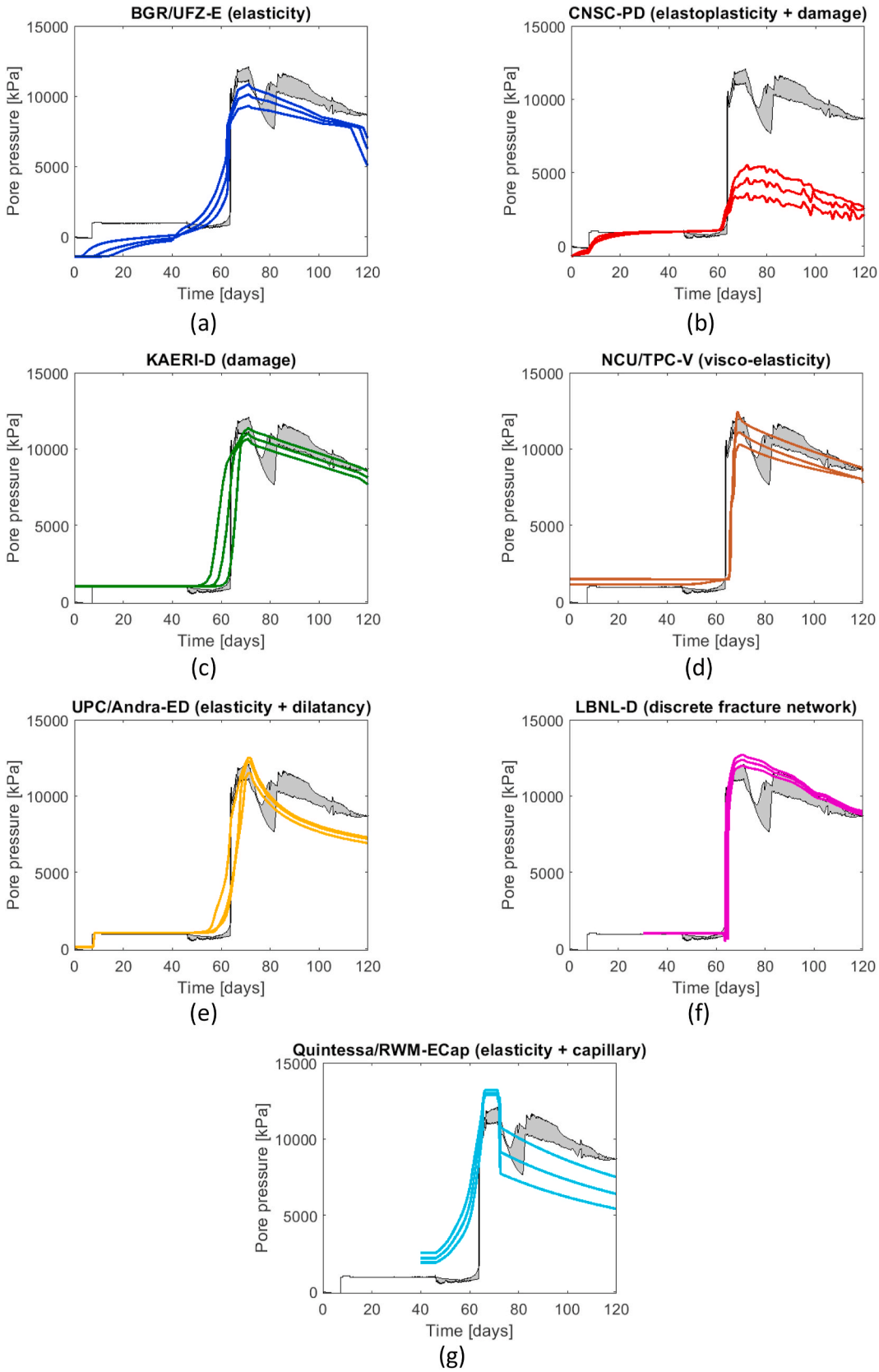

Fig. 16. Experiment 1: experimental versus numerical pore pressures, obtained with models (a) BGR/UFZ-E, (b) CNSC-PD, (c) KAERI-D, (d) NCU/TPC-V, (e) UPC/Andra-ED, (f) LBNL-D and (g) Quintessa/RWM-ECap. All approaches except Quintessa/RWM-ECap are two-phase models and hence, pore pressure can be a combination of both gas and water values.

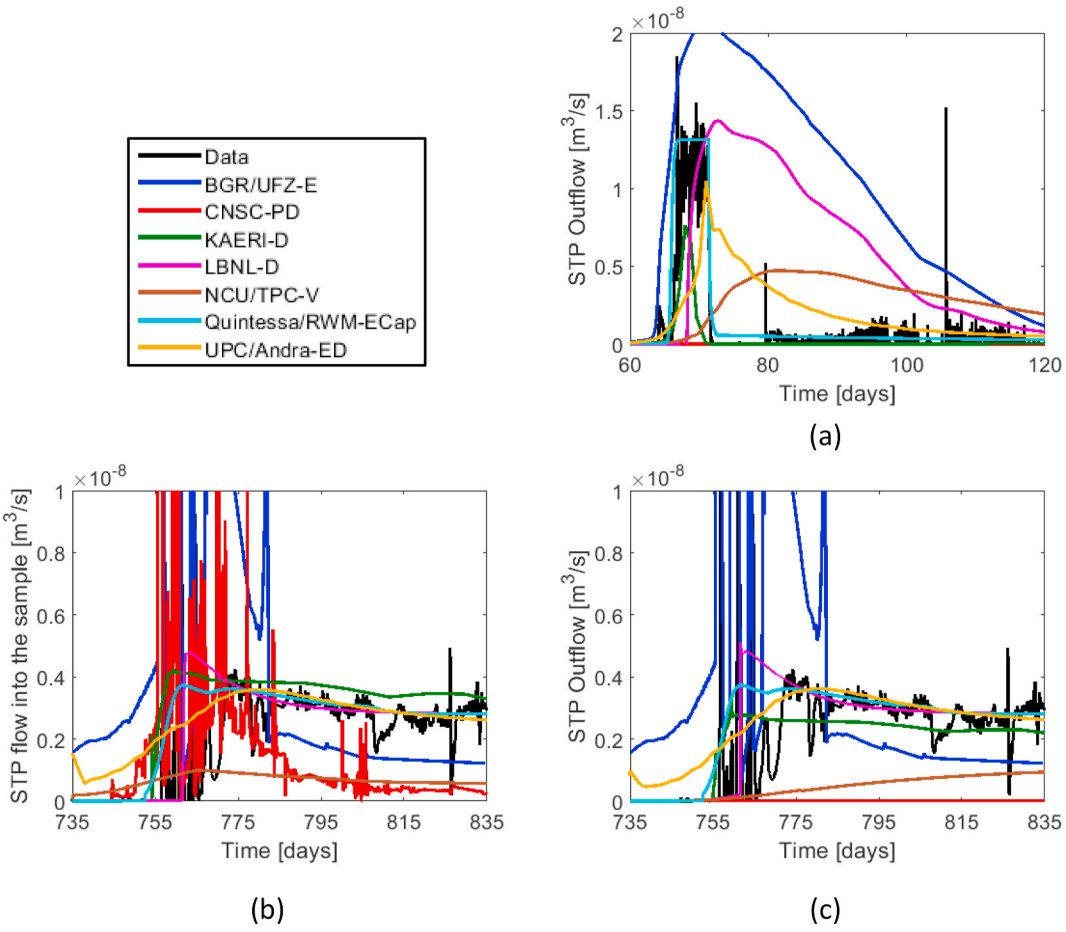

Fig. 17. Comparison of modelled versus observed (a) outflow (experiment 1), (b) inflow (experiment 2) and (c) outflow (experiment 2) results.

conditions also differ from one model to the other, see Appendix A.3 and Appendix A.4 respectively. Although these differences make the model comparison difficult, their effect on model outputs is not expected to be relevant. However, the role of the model parameters emerges as a key consideration:

- Model constraints: model comparison is extremely difficult due to significant differences in the number of parameters that need to be calibrated in each model. As seen in Appendix A.5, some models such as KAERI-D and NCU/TPC-V need 5 or 7 parameters whereas some of the other models (e.g. UPC/Andra-ED and Quintessa/RWM-ECap) need twice as many parameters to represent the additional processes in those models. The difference is even higher when assessing CNSC-PD model, which requires the calibration of 25 parameters (though a number of these have little impact on model output). These differences lead to models with very different degrees of freedom and thus, their fair comparison is a very complex task. Indeed, the fact that some enhanced models achieve poorer fittings than some classical two-phase flow approaches might be explained by this difference in model constraints.
- Parameter calibration: teams calibrate their parameters against different quantities. For instance, CNSC-PD calibrates two different damage parameters (strain at tensile strength and the maximum intrinsic permeability) by means of the inflow magnitude, three additional parameters (consolidation pressure at saturation, reference pressure for BBM and the swelling index at saturation) are calibrated by using the breakthrough pressure, while the inflow curves and the stress evolution are used to calibrate four other parameters. The same stress evolution is used by NCU/TPC-V to calibrate the intrinsic permeability of water, the gas compressibility and the visco-elastic parameters while Quintessa/RWM calibrates its model by using the gas flow rate and the injection pressure.

Table 5
Parameter values that differ from experiment 1 and experiment 2.

Parameter	Units	Value in experiment 1	Value in experiment 2
KAERI-D			
Swelling pressure	MPa	5.5	7.1
Maximum intrinsic permeability	m^2	1.0×10^{-19}	5.0×10^{-19}
LBNL-D			
Biot's coefficient	–	1	–
Swelling coefficient	–	0.1	–
Pore compressibility	Pa^{-1}	2.22×10^{-8}	4.44×10^{-9}
Tensile strength	Pa	1.0×10^{5}	1.0×10^{3}
Cohesive strength	Pa	1.0×10^{5}	4.0×10^{4}
Internal friction angle	deg	18	4.5
Residual gas saturation	–	0.0877	0.0709
Quintessa/RWM-ECap			
Biot's coefficient	–	0.4	0.3
Compressibility of capillaries	$m^2\ Pa^{-1}$	1.0×10^{-18}	1.0×10^{-19}
Reference stress for capillary compressibility	MPa	1.2	0.0

Some of these parameters (e.g. damage smoothing coefficients, capillary spacing …) are purely numerical (i.e. not physically quantified) while others (e.g. tensile strength, swelling pressure …) have a clear physical meaning but experimental data is not available. Hence,

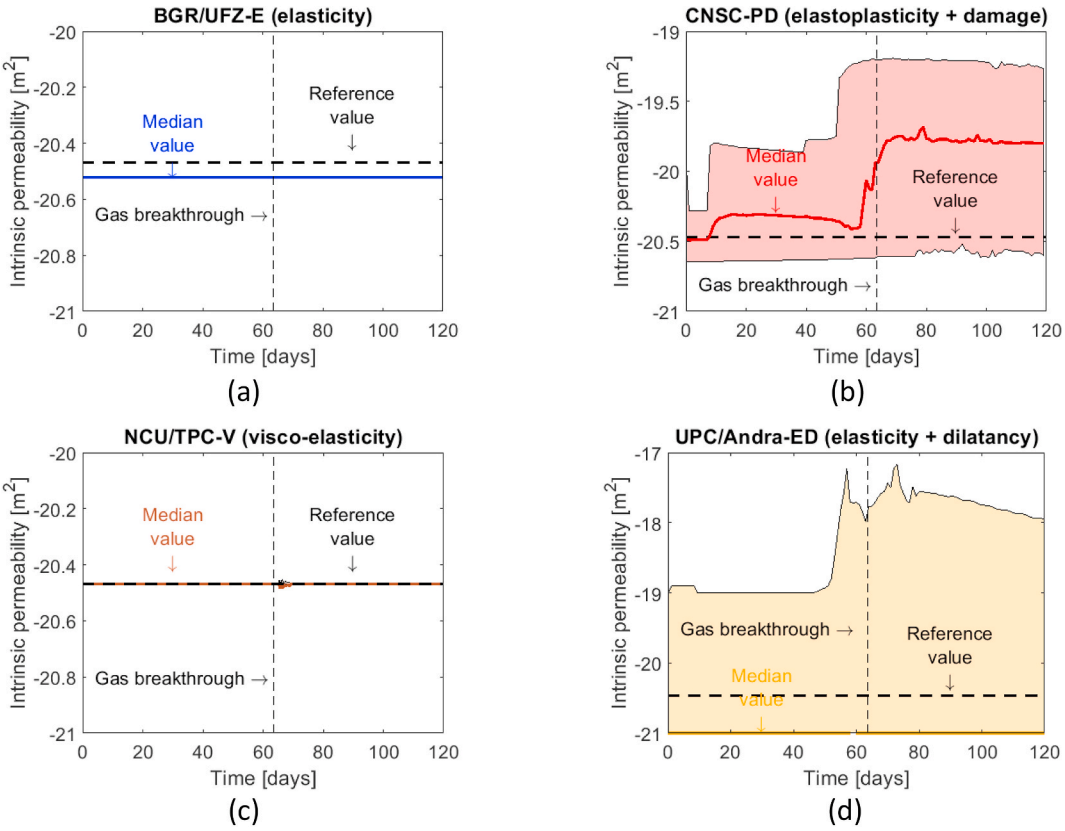

Fig. 18. Experiment 1: intrinsic permeability values used in models (a) BGR/UFZ-E, (b) CNSC-PD, (c) NCU/TPC-V and (d) UPC/Andra-ED. Note that the rest of the teams did not provide these values, in some instances because they were not directly applicable to their models.

their definition is complex. Besides, teams use different values for the same parameter to fit their models (see Appendix A.5) and thus, extrapolation of these calibrations to other tests can be difficult.

- Test differences: some models, see Table 5, assume different parameter values for experiment 1 and experiment 2. Although material heterogeneity could explain some of these differences, huge discrepancies are found, thus indicating that some physical details are not well captured by the models and they need to be fully understood before using the models as a predictive tool to assess gas movement.
- Non-realistic descriptions: in order to match key aspects of the evolution, some models require intrinsic permeability values beyond the specified parameters for the material, see Fig. 18 and Fig. 19. This suggests that the physical description of the system is not fully understood and needs further enhancement: indeed, these parameters are being used to represent different physical processes than what they would be traditionally used for, by correcting permeability for the dilatant gas flow, which may cause issues representing non-dilatant flows through the original pore space.
- Final gas saturations: another difference between models that still needs to be properly understood is their obtained final gas saturation. Indeed, assuming the ideal gas law and neglecting swelling or damage induced changes in porosity (thus, a constant bulk porosity of 0.44 can be used), final gas saturations are derived, see Table 6. As seen, some high gas saturations are obtained, suggesting that either the capillary relationship governing desaturation is incorrect or too many pathways (with too high permeability) are present in the model.

Other key considerations may need to be made depending on the intended usage of the models:

- Heterogeneity: only two models (CNSC-PD and UPC/Andra-ED) include material heterogeneity. However, it needs to be considered in more detail since it might provide one possible route to represent localisation of flow.
- Stochasticity: all the developed models are deterministic. However, the experimental data exhibit a combination of stochastic behaviour (which would be expected to differ if a similar experiment were to be conducted again) and deterministic behaviour. Indeed, although gas entry is well understood, gas breakthrough occurs relatively soon after and depends on the boundary conditions of the test (e.g. the positions of the sink arrays) and stability of gas pathways. Hence, to enhance predictive modelling capability of future models, it is necessary to know more about bentonite and the reproducibility of these experimental results.
- Uncertainty analysis: associated uncertainties from the experimental data need to be further understood. These include the distinction between stochastic and deterministic features (as noted above) and the understanding of the general process associated with gas flow by only looking at these two related experiments. One way of resolving

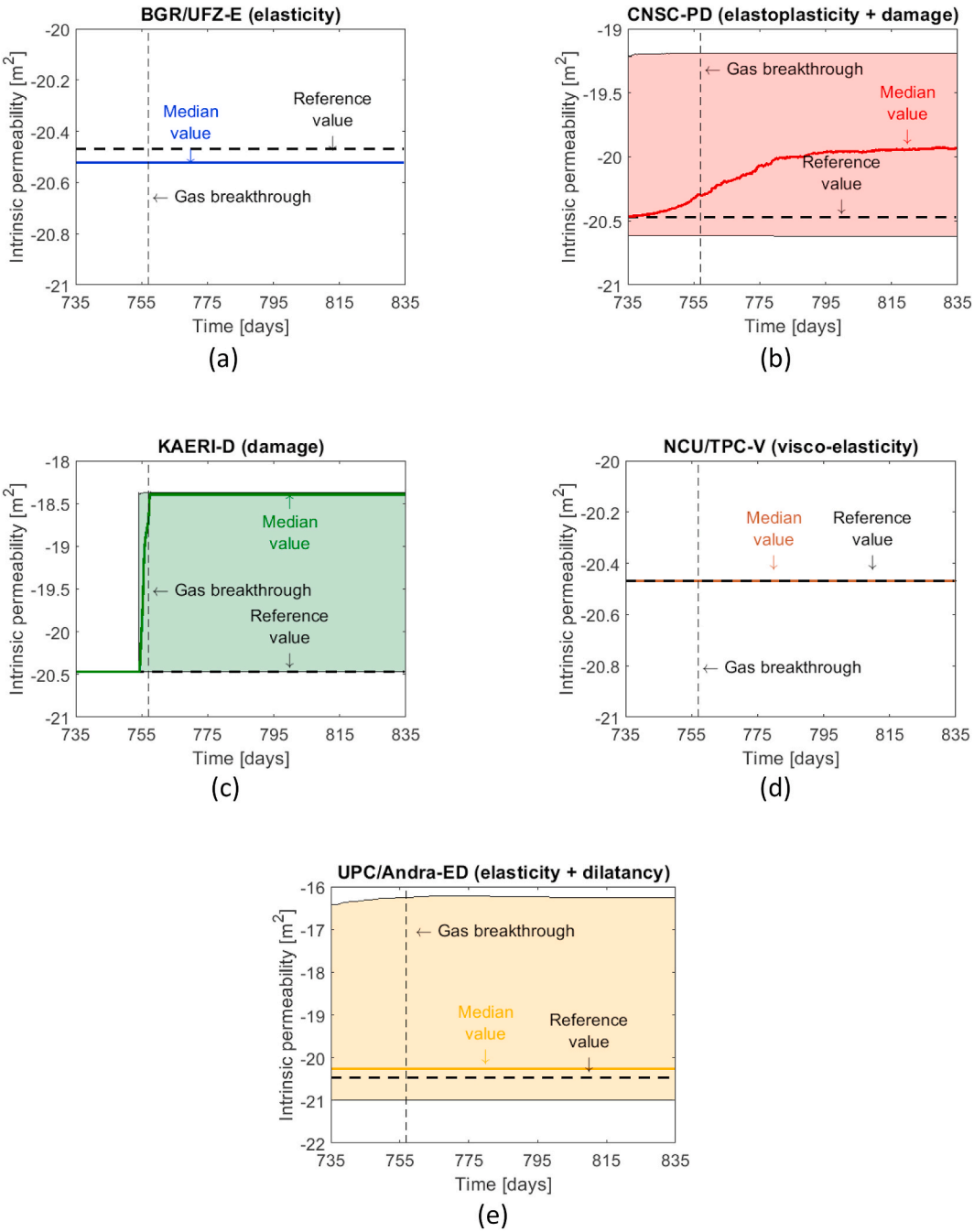

Fig. 19. Experiment 2: intrinsic permeability values used in models (a) BGR/UFZ-E, (b) CNSC-PD, (c) KAERI-D, (d) NCU/TPC-V and (e) UPC/Andra-ED. Note that the rest of the teams did not provide these values, in some instances because they were not directly applicable to their models, and thus, a complete comparison is not possible.

Table 6
Final gas saturations obtained from final STP gas volume (assuming an ideal gas, a constant bulk porosity of 0.44 and a final gas pressure). Note that some teams did not provide these values and thus, a complete comparison is not possible.

Model	Final STP gas volume (m^3)	Number of moles (mol)	Final gas volume (m^3)	Gas saturation (%)
Experiment 1 (final gas pressure of 9.3 MPa)				
BGR/UFZ-E	6.00×10^{-5}	2.68×10^{-3}	7.02×10^{-7}	0.47
CNSC-PD	9.35×10^{-3}	4.17×10^{-1}	1.09×10^{-4}	73.27
NCU/TPC-V	3.97×10^{-5}	1.77×10^{-3}	4.65×10^{-7}	0.31
Quintessa /RWM-ECap	1.02×10^{-11}	4.57×10^{-10}	1.20×10^{-13}	8.03×10^{-8}
UPC/Andra-ED	2.14×10^{-3}	9.55×10^{-2}	2.50×10^{-5}	16.77
Experiment 2 (final gas pressure of 8.1 MPa)				
BGR/UFZ-E	1.68×10^{-4}	7.50×10^{-3}	2.26×10^{-6}	1.51
CNSC-PD	5.90×10^{-3}	2.64×10^{-1}	7.93×10^{-5}	53.13
KAERI-D	8.69×10^{-3}	3.88×10^{-1}	1.17×10^{-4}	78.20
LBNL-D	2.77×10^{-4}	1.24×10^{-2}	3.72×10^{-6}	2.49
NCU/TPC-V	2.41×10^{-5}	1.08×10^{-3}	3.24×10^{-7}	0.22
Quintessa/ RWM-ECap	9.33×10^{-11}	4.16×10^{-9}	1.25×10^{-12}	8.39×10^{-7}
UPC/Andra-ED	1.53×10^{-3}	6.83×10^{-2}	2.06×10^{-5}	13.77

some of these uncertainties and building confidence in the process models would be to look at other similar experimental datasets. Note though that the level to which some of these uncertainties need to be resolved will depend on the requirements from the intended usage (e.g. for a repository safety case).

6. Conclusions

This paper presents a summary of work performed in Task A of the DECOVALEX-2019 phase in which 8 teams have attempted to model the movement of gas in plastic clays in 1D and 3D experiments performed under controlled laboratory conditions.

The experimental data from these gas injection tests exhibit a combination of stochastic and deterministic behaviours. The observed breakthrough after a period of increasing gas pressure and bulk gas flow through a main emergent pathway are common to the 1D and 3D experiments. The instability and pathway switching observed in the 3D experiment before a main flow path is established, suggests that the precise timing of the gas breakthrough and associated gas flows may be stochastic by nature. It is therefore important for numerical modelling to understand and distinguish between the key experimental features reproducible across all experiments and those that only occur in specific experiments. This is also an area where other similarly high-quality experimental datasets would be useful to help give confidence in the process of understanding. It is also important to recognise that different modelling approaches have different objectives in terms of their intended application. The results of models need to be judged against their stated objectives rather than the full detail of the experiments, the specifics of which may or may not be significant for the application. Even simple models can have an intrinsic value and can also give insights into the representation of the complex phenomenological behaviour exhibited in the experiments.

Four types of modelling approaches have been developed: (i) two-phase flow models coupled to a range of different mechanical deformation behaviours, (ii) enhanced two-phase flow models in which fractures are embedded within a plastic material (continuous techniques) or incorporated into the model using a rigid-body-spring network (discrete approaches), (iii) a single-phase model incorporating a creep damage function in which only gas flow is considered, and (iv) a conceptual approach used to examine the chaotic nature of gas flow.

In contrast to previous international gas projects such as EVEGAS or GAMBIT, application of standard two-dimensional and three-dimensional two-phase flow models shows that they are capable of obtaining some good fittings with respect to experimental stress and pore pressure measurement results. However, these models do not reflect some of the important underlying physics (e.g. creation of dilatant pathways) associated with advective gas flow and are therefore unable to describe the full complexity of the processes in such low-permeability materials. They require substantial calibration of fitting parameters and do not reproduce the dynamic behaviour observed in the experiments.

Continuous approaches with preferential pathways have less constraints within the models and while they fail in fitting some experimental details, the phenomenological processes presented better reflect the mechanisms controlling advective gas flow. Similarly, discrete models, whose basis reflects the underlying physics of gas flow, also struggle to capture some of the key experimental features of the data. However, from a pragmatic perspective, continuous enhanced two-phase flow and discontinuous models provide a viable framework to develop numerical tools to represent these complex physical processes, and ultimately provide a tool which can represent different data/boundary conditions without major recalibration. However, while much work is required to achieve this goal, outputs from the models continue to provide insight into the physical processes controlling the advection of gas.

Simple enhanced flow models (such as single-phase flow models) can also be employed. They have been proven to reproduce some of the key deterministic features of the experiments without attempting to capture all stochastic experimental behaviour. When considering the potential need to model at scales greater than the small experiments considered in this work (the experiment scale is at least a factor 10 below the scale of interest), they may provide a useful starting point for deriving new models that are tractable at repository scales.

New conceptual models such as the SNL model may be hence developed to explain this complexity. However, results from this task show that their development is still in a very preliminary phase and at the current stage of the work, they are not able to reproduce the experiments or processes in a comprehensive way. Thus, from a pragmatic perspective, enhanced flow models (either by different deformation behaviours, explicitly incorporating different pathways and/or evolving fractures) are a viable tool to represent these systems. However, the complexity of the physical processes combined with detailed calibration processes, currently limit their use in the quantitative prediction of gas flow and (if necessary) should be used with extreme caution. However, they are a necessary step towards building understanding of the important experimental phenomena. Thus, and depending on the intended usage of the models, in the application of these approaches, calibration of parameters, constraints and parameterisation of the codes, as well as the description of number, density and aperture distributions of the gas pathways, all emerge as key considerations in the modelling of advective gas.

Declaration of competing interest

The authors declare that they have no known competing financial interests or personal relationships that could have appeared to influence the work reported in this paper.

Acknowledgements

DECOVALEX is an international research project comprising participants from industry, government and academia, focusing on development of understanding, models and codes in complex coupled problems in sub-surface geological and engineering applications; DECOVALEX-2019 is the current phase of the project. The authors appreciate and thank the DECOVALEX-2019 funding organisations Andra, BGR/UFZ, CNSC, US DOE, ENSI, JAEA, IRSN, KAERI, NWMO, RWM, SÚRAO, SSM and Taipower for their financial and technical support of the work described in this paper. The statements made in the paper are, however, solely those of the authors and do not necessarily reflect those of the funding organisations.

Appendix A. Model comparison

Differences between the proposed strategies lie in the software used by the teams (Table 7), in the assumed geometry to represent the saturated bentonite (Table 8), in the prescribed initial conditions (Tables 9 and 10), in the prescribed boundary conditions (Tables 12 and 13), in the material parameters and in their main objectives. These differences make it difficult to carry out direct comparison.

A.1. Codes

BGR/UFZ implemented the BGR/UFZ-E model using the OpenGeoSys (OGS) code. This is a scientific open source project for the development of numerical methods for the simulation of thermo-hydro-mechanical-chemical (THMC) processes in porous and fractured media. Model CNSC-PD is implemented in COMSOL Multiphysics®. This software is also used by KAERI to numerically simulate experiment 2. However, it uses TOUGH2-FLAC3D to simulate the one-dimensional test. NCU/TPC-V uses a three-dimensional in-house thermo-hydro-mechanical-chemical software to numerically simulate both experiments. Another in-house code is used by UPC/Andra, who uses the Code_bright code to simulate both experiments. LBNL uses TOUGH coupled to the RBSN whereas Quintessa/RWM implemented Quintessa/RWM-ECap model using the QPAC code, Quintessa's in-house general-purpose modelling software.

Table 7
Software used by the participating teams.

Model	Software	Version	Reference
BGR/UFZ-E	OpenGeoSys	5.8	26
CNSC-PD	COMSOL Multiphysics®	5.4	56
KAERI-D	Experiment 1: TOUGH2/FLAC3D	–	47,57
	Experiment 2: COMSOL Multiphysics®	–	56
NCU/TPC-V	THMC	7.1	37,38,42
UPC/Andra-ED	Code_bright	8.6	58
LBNL-D	TOUGH-RBSN	–	59
Quintessa/RWM-ECap	QPAC	4.2	60,61

A.2. Test geometries

Different test geometries have been used by the participating teams.

To simulate the one-dimensional test (experiment 1), BGR/UFZ-E uses a triangular two-dimensional axi-symmetric mesh, whereas a hexahedral three-dimensional mesh was generated for the spherical test (experiment 2), see Fig. 20. Model CNSC-PD uses different triangular finite element meshes: (i) a two-dimensional axi-symmetrical mesh and (ii) a three-dimensional mesh, see Figs. 21 and 22. KAERI-D uses different discretisation methods: (i) a three-dimensional finite difference grid has been used for experiment 1 and (ii) a three-dimensional finite element mesh for experiment 2. NCU/TPC-V uses a finite element mesh of more than 7000 hexahedral elements with more than 8000 nodes, see Fig. 23.

UPC/Andra implemented the one-dimensional test (experiment 1) using the three-dimensional finite element mesh of Fig. 24a, whereas for experiment 2, the mesh of Fig. 24b was employed. As seen in Fig. 24, UPC/Andra-ED model is heterogeneous. This heterogeneity has been represented through the intrinsic permeability distribution, which generates a porosity field that changes in space and time. Indeed, three different initial intrinsic soil permeabilities have been assigned to material volumes. The modelled sample is divided by 12 layers and each layer is composed by 64 volumes. Despite for the two tests the general methodology and material properties are the same, the material assignation for experiment 1 and experiment 2 is different:

- Experiment 1 model (Fig. 24a): 1 layer was selected with about a random 1/6 weighting distribution for $k_0 = 1 \times 10^{-19}$ m^2 (higher permeability), 1/6 for $k_0 = 1 \times 10^{-20}$ m^2 and 2/3 for $k_0 = 1 \times 10^{-21}$ m^2 (lower permeability). The subsequent 11 layers are also randomly generated. This has been achieved by rotating 1 turning step layer-by-layer, and thus, a kind of axial connectivity of the permeability is generated.
- Experiment 2 model (Fig. 24b): a random permeability distribution is also assigned layer-by-layer. The same weighting as before is used. However, no rotation assignation (i.e., no forced connectivity assignation) is prescribed, which is in line with the test features (i.e., spherical flow dissipation).

LBNL-D model uses a two-dimensional finite volume grid to simulate experiment 1 (see Fig. 25) and a three-dimensional finite volume mesh for

experiment 2, see Fig. 26.

Quintessa/RWM-ECap uses a one-dimensional finite volume grid to simulate experiment 1 (see Fig. 27) and a two-dimensional axi-symmetrical mesh for experiment 2 (Fig. 28).

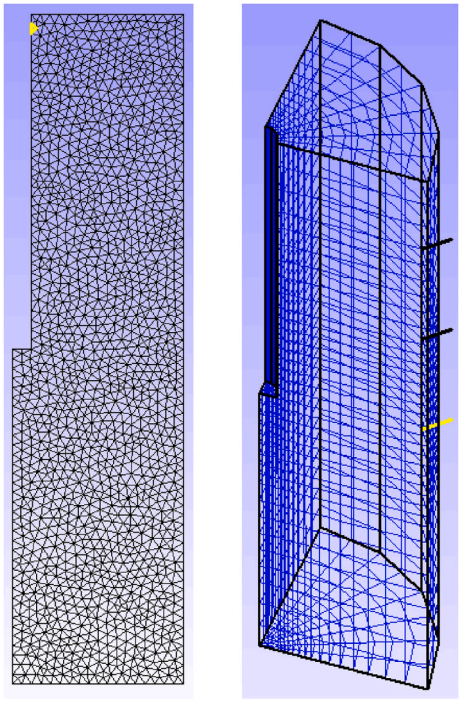

Fig. 20. BGR/UFZ-E model. Finite element mesh for (a) experiment 1 and (b) experiment 2.

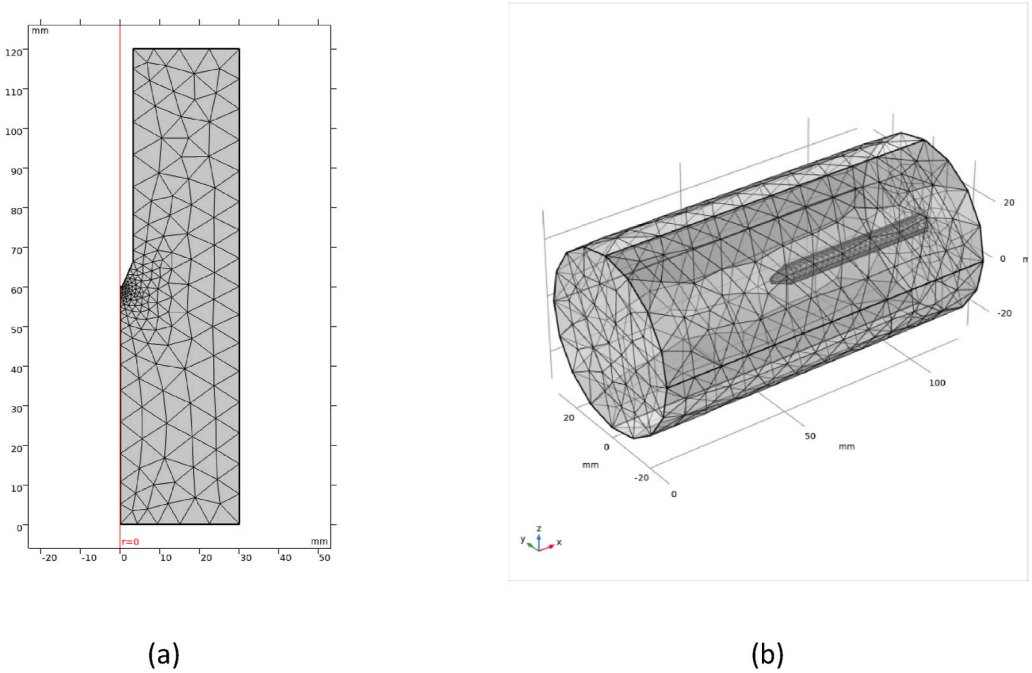

Fig. 21. CNSC-PD model. Finite element meshes used to simulate experiment 1: (a) a two-dimensional axisymmetrical mesh and (b) a three-dimensional mesh.

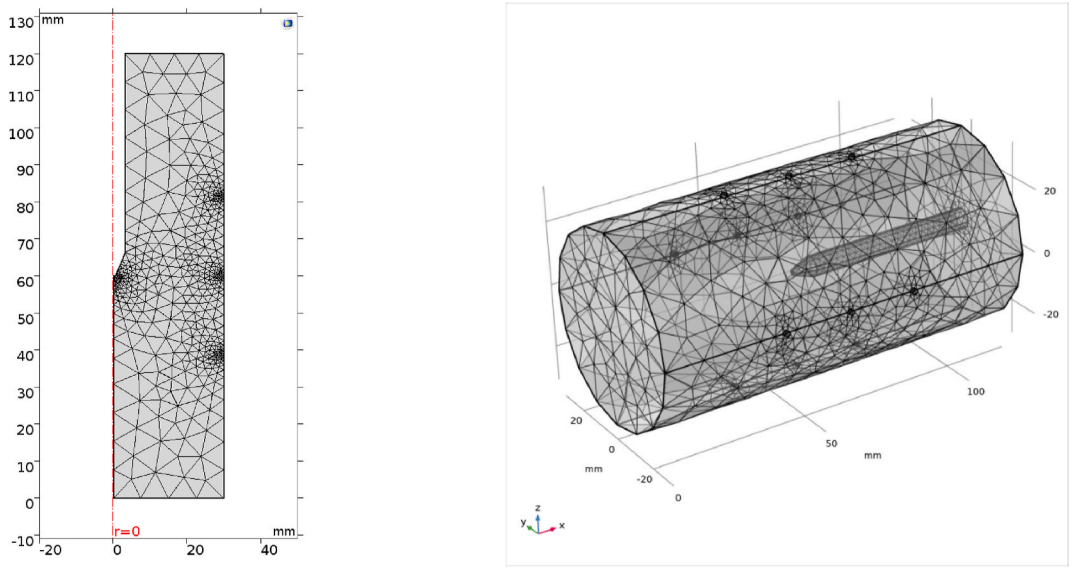

Fig. 22. CNSC-PD model. Finite element meshes used to simulate experiment 2: (a) a two-dimensional axisymmetrical mesh and (b) a three-dimensional mesh.

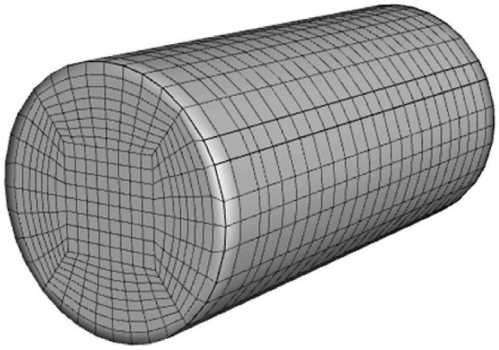

Fig. 23. NCU/TPC-V model. Finite element mesh used for experiment 1 and experiment 2.

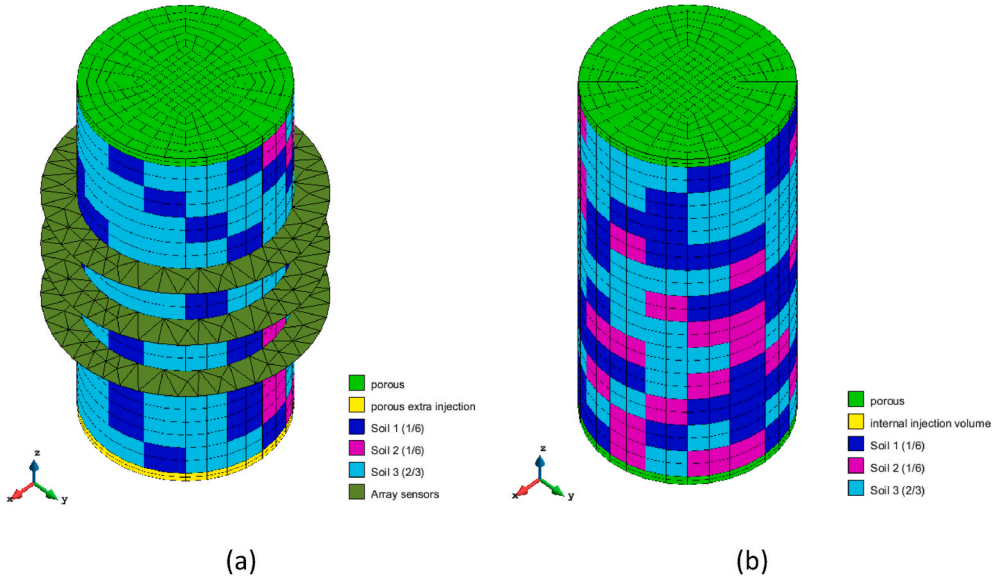

Fig. 24. UPC/Andra-ED model. Finite element meshes and materials assumed for (a) experiment 1 and (b)experiment 2. (Note: Soils 1-2-3 coloured assignation is related to initial intrinsic permeability values).

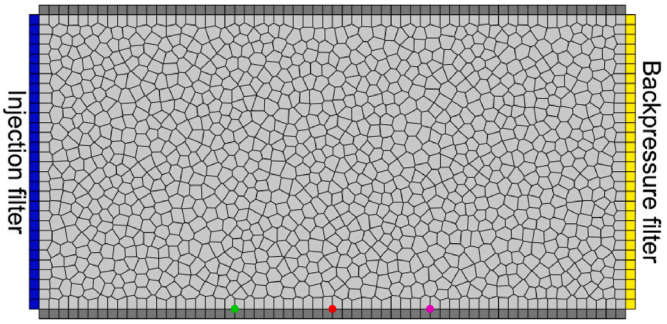

Fig. 25. LBNL-D model. Two-dimensional rectangular grid for experiment 1.

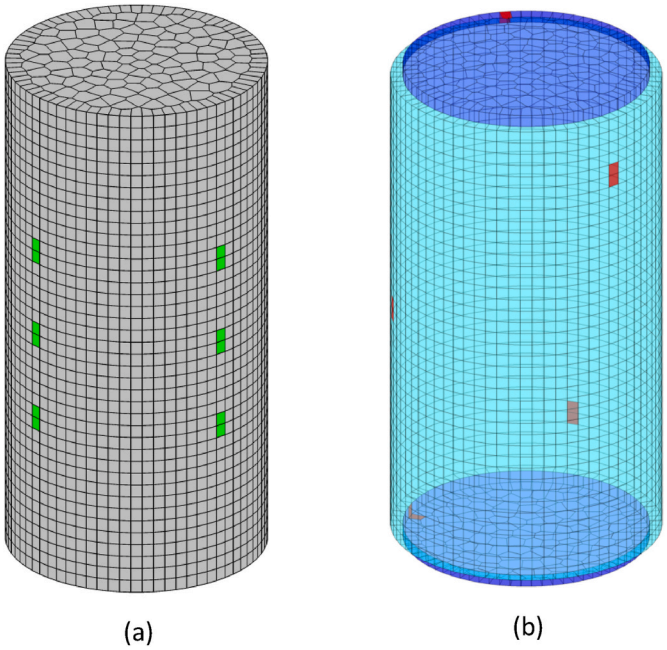

Fig. 26. LBNL-D model. (a) Three-dimensional mesh for experiment 2.6 Green marks (and 6 hidden on the other side) indicate the locations of porewater sensors for outflow measurement. (b) Outer elements are padded for zero-displacement constraints. Red marks indicate the location of load cells, where the local stress values are measured.

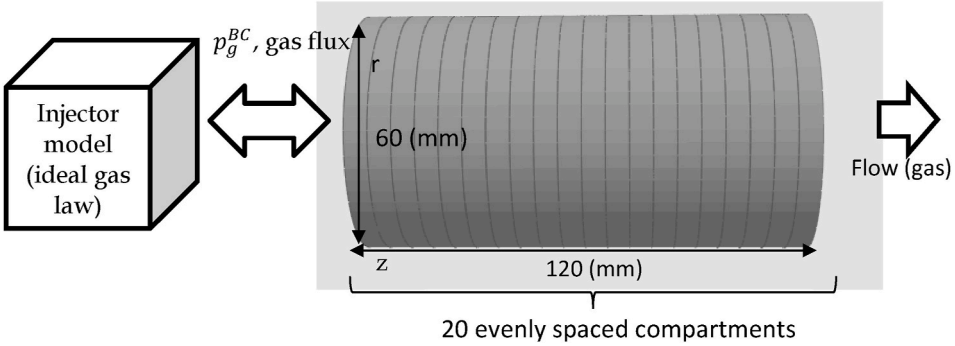

Fig. 27. Quintessa/RWM-ECap model. Schematic discretisation used for experiment 1.

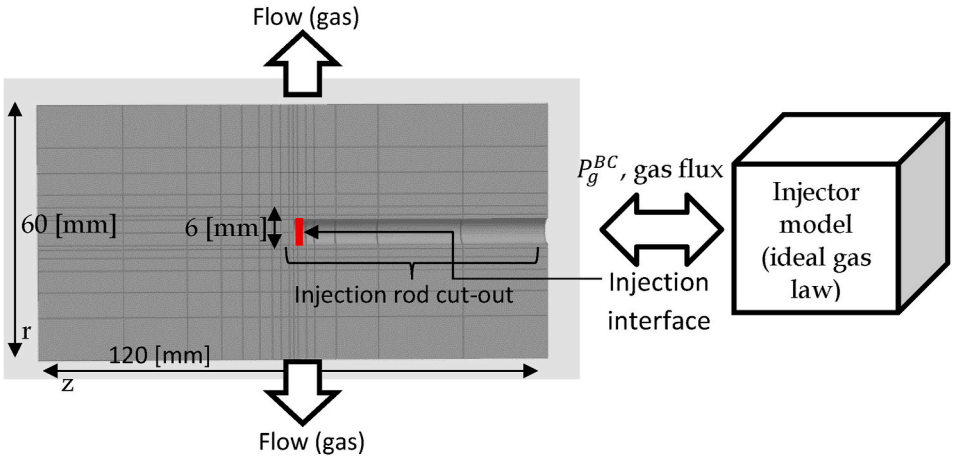

Fig. 28. Quintessa/RWM-ECap. Schematic discretisation used for experiment 2.

Table 8
Test geometries used by the participating teams. Note that TRI stands for traingles, HEX for hexahedra, TET for tetrahedra, QUAD for quadrilaters, POLY for polyhedral and ORT for orthogonal cylindrical

Model	Test	Discretisation method	Geometry	Sample discretisation	
				type of elements	# of nodes
BGR/UFZ-E	1D	Finite element	2D	TRI	1448
	3D	Finite element	3D	HEX	5635
CNSC-PD	1D	Finite element	2D axisym.	TRI	~850
			3D	TET	~31,000
	3D	Finite element	2D axisym.	TRI	~2000
			3D	TET	~500,000
KAERI-D	1D	Finite difference	3D	HEX	7560
	3D	Finite element	3D	TET for bentonite HEX for filters QUAD for the interface	7961
NCU/TPC-V	3D	Finite element	3D	HEX	8425
	3D	Finite element	3D	HEX	8425
UPC/Andra-ED	1D	Finite element	3D	HEX for bentonite TRI for sensors	8205
	3D	Finite element	3D	HEX for bentonite TRI for sensors	7920
LBNL-D	1D	Finite volume + lattice spring elements	2D	POLY	1401
	3D	Finite volume + lattice spring elements	3D	POLY	7856
Quintessa/RWM-ECap	1D	Finite volume	1D	ORT	Cell-centred nodes in FV (# of cells: 20)
	3D	Finite volume	2D axisym.	ORT	Cell-centred nodes in FV (# of cells: 105)

A.3. Initial conditions

Different initial conditions are assumed by the modelling teams.
BGR/UFZ-E assumes the following initial conditions for both experiments:

- **Hydraulic conditions**: gas pressure is prescribed to 1 MPa, capillary pressure is prescribed to 1.875 MPa and water saturation is set to 0.96.
- **Mechanical conditions**: displacements at all axis are set to 0.
- **Other conditions**: temperature is prescribed at 20 °C.

CNSC/PD-E assumes the following conditions for experiment 1:

- **Hydraulic conditions**: gas pressure is prescribed to 1.01×10^5 Pa, water pressure is prescribed to -5.7×10^6 Pa and water saturation is set to 0.96.
- **Mechanical conditions**: displacements at all axis are 0. The initial stress tensor is assumed to be diagonal with coefficients $\sigma_{0xx} = \sigma_{0yy} = \sigma_{0zz} = 2.0 \times 10^5$ Pa

- **Other conditions**: temperature is prescribed at 25 °C.

whereas for the spherical test (experiment 2), it assumes.

- **Hydraulic conditions**: gas pressure is prescribed to 1.53 MPa, water pressure is prescribed to 1 MPa and water saturation is set to 1.00.
- **Mechanical conditions**: displacements in all axes are 0. The initial stress tensor is assumed to be diagonal with coefficients $\sigma_{0xx} = \sigma_{0yy} = \sigma_{0zz} =$ 6.5 MPa.
- **Other conditions**: temperature is prescribed at 25 °C.

KAERI-D also assumes different initial conditions for the one-dimensional test (experiment 1) and for the three-dimensional test (experiment 2). Indeed, for experiment 1:

- **Hydraulic conditions**: water and gas pressures are prescribed to 1 MPa, water saturation is 0.98.
- **Mechanical conditions**: displacements at all axis are 0. The initial stress tensor is assumed to be diagonal with coefficients $\sigma_{0xx} = \sigma_{0yy} = \sigma_{0zz} =$ 5.5 MPa and the swelling pressure is set to 5.5 MPa.
- **Other conditions**: temperature is prescribed at 10 °C.

whereas for experiment 2:

- **Hydraulic conditions**: water and gas pressures are prescribed to 1 MPa, water saturation is set to 0.98.
- **Mechanical conditions**: displacements at all axis are set to 0. The initial stress tensor is assumed to be diagonal with coefficients $\sigma_{0xx} = \sigma_{0yy} = \sigma_{0zz} = 7.1$ MPa and the swelling pressure is set to 7.1 MPa.
- **Other conditions**: temperature is prescribed at 20 °C.

In NCU/TPC-V, the initial conditions for the one-dimensional test (experiment 1) and the three-dimensional test (experiment 2) are.

- **Hydraulic conditions**: water pressure is prescribed to 1 MPa, gas pressure is prescribed to 3 MPa and water saturation is 0.99. Initial porosity is prescribed to 0.43, initial solid density is 1600 kg/m^3 and the initial intrinsic permeability is 3.4×10^{-21} m^2.
- **Mechanical conditions**: displacements at all axis are 0. The initial stress tensor is also set to 0 MPa and the swelling pressure is 0 MPa.

In UPC/Andra-ED, the initial conditions for the one-dimensional test (experiment 1) and the three-dimensional test (experiment 2) are.

- **Hydraulic conditions**: water and gas pressures are prescribed to 0.1 MP and water saturation is 1. Initial porosity is prescribed to 0.44.
- **Mechanical conditions**: displacements at all axis are 0. The initial stress tensor is assumed to be diagonal, with $\sigma_x = \sigma_y = 5$ MPa and $\sigma_z = 8$ MPa.
- **Other conditions**: temperature is prescribed to 20 °C.

Same hydraulic conditions are assumed for experiment 2. However, for the three-dimensional test, isotropy is considered and the initial stress tensor is assumed to be diagonal with coefficients $\sigma_{0xx} = \sigma_{0yy} = \sigma_{0zz} = 4$ MPa.

In both cases, Henry's law is assumed to define gas concentration in water.

In LBNL-D, the prescribed initial conditions are.

- **Hydraulic conditions**: in experiment 1, water pressure is prescribed to 0.98228 MPa, gas pressure is set to 1 MPa and water saturation to 0.9999. In experiment 2, water and gas pressures are prescribed to 1 MPa and water saturation to 1.
- **Mechanical conditions**: in experiment 1, axial stress is set to 9 MPa and radial components to 6 MPa. In experiment 2, axial stress is set to 7.250 MPa and radial components to 7.750 MPa.
- **Other conditions**: temperature is prescribed to 20 °C in both experiments.

and in Quintessa/RWM-ECap, they are:

- **Hydraulic conditions**: gas pressure is prescribed balanced with boundary conditions.
- **Mechanical conditions**: stress tensor is prescribed. Indeed, in experiment 1, axial stress is set to 9.5 MPa and in experiment 2–7.25 MPa. Radial components are set to 7.25 MPa in experiment 2 whereas for experiment 1, the function

$$\sigma_{rr}(z, t_0) = 7\ [\text{MPa}] - (z - 15\ [\text{mm}]) \left(\frac{0.5\ [\text{MPa}]}{45\ [\text{mm}]} \right) \tag{65}$$

is assumed to replicate the experimental stresses at t_0. Pore pressure is prescribed to 1 MPa in both experiments.

- **Other conditions**: in both experiments, temperature is prescribed to 20 °C, capillary diameter is prescribed to 0.1 μm and $\theta_{creep} = 1 \times 10^{-10}$ for negligible flow at t_0. In experiment 1, initial time is set to 39 days and in experiment 2, to 700 days

Table 9
Experiment 1: initial conditions prescribed by the participating teams.

	Model						
	BGR/UFZ-E	CNSC-PD	KAERI-D	NCU/TPC-V	UPC/Andra-ED	LBNL-D	Quintessa/RWM-ECap
Pore-water pressure (MPa)		−5.7	1	1	0.1	0.98228	
Pore-gas pressure (MPa)	1	0.101	1	3	0.1	1	Balanced with boundary conditions
Water saturation (%)	96	96	98	99	100	99.99	
Displacement along x axis (m)	0	0	0	0	0		0
Displacement along y axis (m)	0	0	0	0	0		0
Displacement along z axis (m)		0	0	0	0		0
Stress tensor (MPa)		0.2·**I**	5.5·**I**	0·**I**	$\begin{pmatrix} 5 & 0 & 0 \\ 0 & 5 & 0 \\ 0 & 0 & 8 \end{pmatrix}$	$\sigma_{zz} = 9$ $\sigma_{rr} = 6$	$\sigma_{zz} = 9.5$ σ_{rr} = linear function
Swelling pressure (MPa)			5.5	0			
Temperature (°C)	20	25	10	25	20	20	20

Table 10
Experiment 2: initial conditions prescribed by the participating teams.

	Model						
	BGR/UFZ-E	CNSC-PD	KAERI-D	NCU/TPC-V	UPC/Andra-ED	LBNL-D	Quintessa/RWM-ECap
Pore-water pressure (MPa)		1	1	1	0.1	1	
Pore-gas pressure (MPa)	1	1.53	1	3	0.1	1	Balanced with boundary conditions
Water saturation (%)	96	100	98	99	100	100	
Displacement along x axis (m)	0	0	0	0	0		0
Displacement along y axis (m)	0	0	0	0	0		0
Displacement along z axis (m)		0	0	0	0		0
Stress tensor (MPa)		6.5·**I**	7.1·**I**	0·**I**	4·**I**	$\sigma_{zz} = 7.25$ $\sigma_{rr} = 7.75$	$\sigma_{zz} = 7.25$ $\sigma_{rr} = 7.25$
Swelling pressure (MPa)			7.1	0			
Temperature (°C)	20	25	20	25	20	20	20

A.4. Boundary conditions

Different boundary conditions are assumed by the teams.
BGR/UFZ-E assumes the following boundary conditions:

- **Hydraulic conditions**: in experiment 1, gas pressure is prescribed to 1.975 MPa at the top surface and as seen in Fig. 29a at the bottom surface, capillary pressure is prescribed to 1.875 MPa at the top surface and assumed to behave as a step function (see Fig. 29b) at the bottom; in experiment 2, gas pressure is prescribed to 1.975 MPa at the inner surface and a non-linear calibrated function (see Fig. 30a) at the outer surface; capillary pressure is prescribed to 1.875 MPa at the inner surface and assumed to behave as a step function (see Fig. 30b) at the outer boundary. Note that inner and outer surfaces are merely designations for the surfaces formed by the bore around the centre of the bentonite and the outer wall of the bentonite respectively.
- **Mechanical conditions**: a zero-displacement boundary is considered in both experiments.
- **Other conditions**: temperature is prescribed at 20 °C in both experiments.

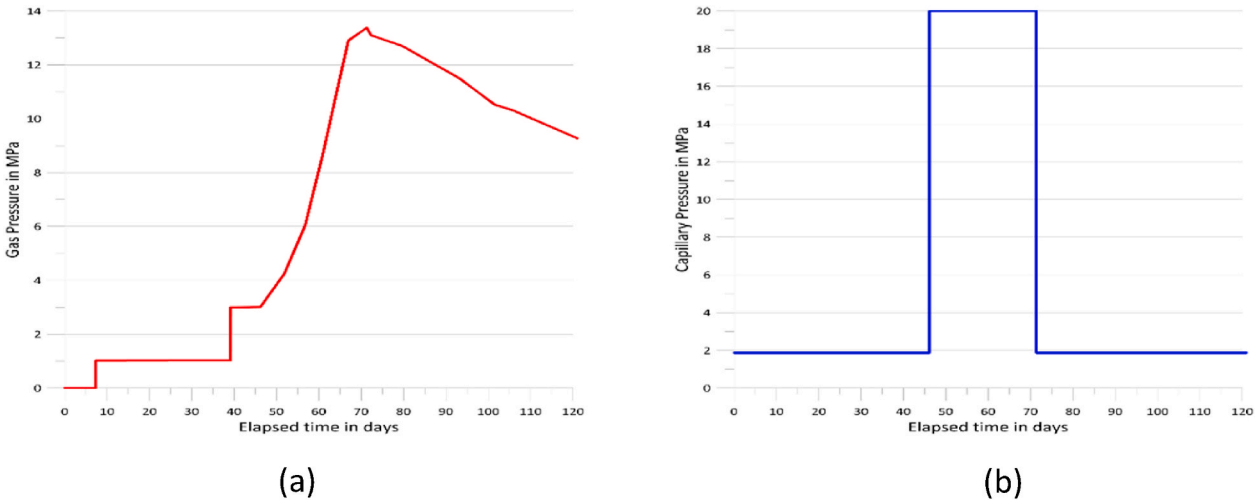

Fig. 29. BGR/UFZ-E model: boundary conditions for experiment 1: prescribed functions for (a) the gas pressure and (b) the capillary pressure.

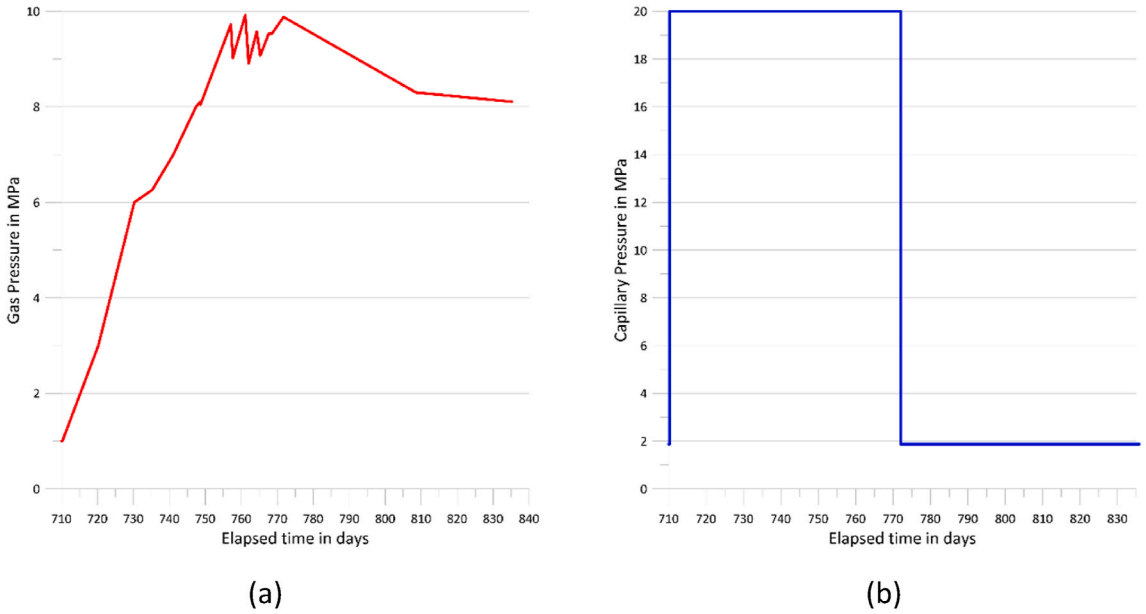

Fig. 30. BGR/UFZ-E model: boundary conditions for experiment 2: prescribed functions for (a) the gas pressure and (b) the capillary pressure.

CNSC-PD model assumes the following boundary conditions for experiment 1:

- **Hydraulic conditions**: pore-gas pressure is prescribed as
  - At lower boundary (A in Fig. 31a and b): $p_g(t)$ = gas injection pressure
  - At lower boundary (A in Fig. 31a and b): $p_g(t)$ = gas injection pressure• At radial boundaries (B in Fig. 31a and b): $\frac{\partial p_g}{\partial x_i} = 0$
  - At upper boundary (C in Fig. 31a and b): $p_g(t)$ = atmospheric[2]

dissolved gas concentration in pore-water (kg gas m^{-3} water) is prescribed as.

- At lower boundary (A in Fig. 31a and b): $c_{g,\,H_2O}(t) = \rho_g(t)H(\varphi S_w)$
- At radial boundaries (B in Fig. 31a and b): $\frac{\partial C_g}{\partial x_i} = 0$
- At upper boundary (C in Fig. 31a and b): $c_{g,\,H_2O}(t) = \rho_g(t)H(\varphi S_w)$

with H (kg species A m^{-3} in aqueous phase kg^{-1} species A m^3 in gas phase) being the Henry's coefficient and pore-water pressure is prescribed as.

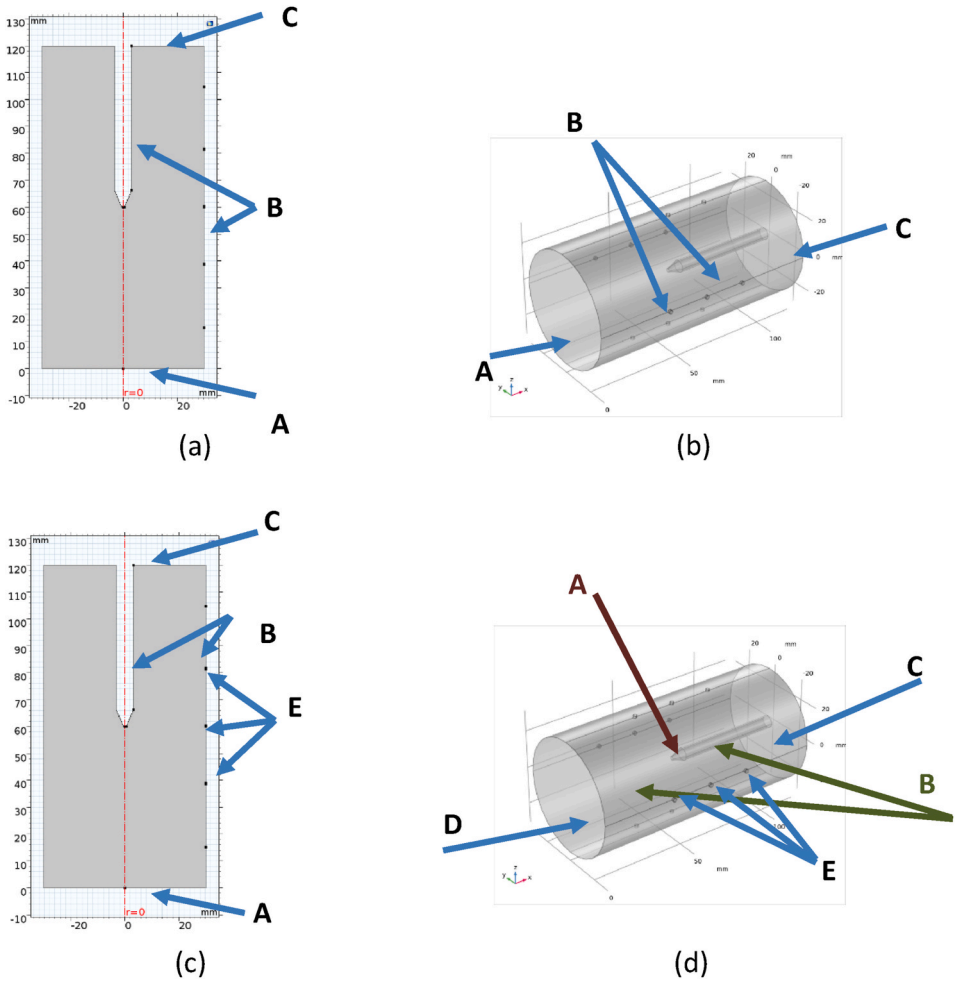

Fig. 31. CNSC-PD model: boundaries where boundary conditions are prescribed for (a) experiment 1 (2D mesh), (b) experiment 1 (3D mesh), (c) experiment 2 (2D mesh) and (d) experiment 2 (3D mesh).

- At lower and radial boundaries (A and B in Fig. 31a and b): $\frac{\partial p_w}{\partial x_i} = 0$
- At upper boundary (C in Fig. 31a and b): $p_w(t) =$ water backpressure (time dependent starting at 0.05 MPa and going up to 1 MPa).
- **Mechanical conditions**: a roller constraint condition is applied everywhere. That is, boundary-free in tangential direction but fixed in normal direction.

CNSC-PD assumes similar conditions for experiment 2:

- **Hydraulic conditions**: pore-gas pressure is prescribed as
  - At middle boundary (A in Fig. 31c and d): $p_g(t) =$ gas injection pressure
  - At radial boundaries, including injection rod but not tip (B in Fig. 31c and d): $\frac{\partial p_g}{\partial x_i} = 0$
  - At upper and lower boundaries (C and D in Fig. 31c and d): $p_g(t) =$ atmospheric[3]

dissolved gas concentration in pore-water (kg gas m^{-3} water) is prescribed as.

- At middle boundary (A in Fig. 31c and d): $c_{g,\,H_2O}(t) = \rho_g(t) H(\varphi S_w)$
- At radial boundaries, including injection rod, but not tip (B in Fig. 31c and d): $\frac{\partial C_g}{\partial x_i} = 0$
- At upper boundary and lower boundaries (C and D in Fig. 31c and d): $c_{g,\,H_2O}(t) = \rho_g(t) H(\varphi S_w)$

with H (kg species A m^{-3} in aqueous phase kg^{-1} species A m^3 in gas phase) being the Henry's coefficient and pore-water pressure is prescribed as.

- At middle, radial and lower boundaries (A, B and D in Fig. 31c and d: $\frac{\partial p_w}{\partial x_i} = 0$

[3] As done in experiment 1, this value will be set to 1 MPa and its impact will be assessed in Dagher E.E., Nguyen T.S. and Infante Sedano J.A. Assessing Mechanisms of Mechanical Deformation to Simulate Two-Phase Flow in a Swelling Geomaterial. (To be submitted to the Special Publication of International Journal of Rock Mechanics and Mining Sciences).

- At upper boundary and at pore-fluid array boundaries (C and E in Fig. 31c and d): $p_w(t) = 1$ MPa
- **Mechanical conditions**: a roller constraint condition is applied everywhere. That is, boundary-free in tangential direction but fixed in normal direction.

For experiment 1, KAERI-D model assumes the following boundary conditions:

- **Hydraulic conditions**: gas and water pressures are prescribed to 1 MPa at the backpressure and radial filters (B and C in Fig. 32a). At these locations, water saturation is prescribed to 0.98. Flowrate is prescribed to 0 m^3/s everywhere except in the injection, backpressure and radial filters and at the injection filter (A in Fig. 32a) is as follows:
  - From 0 to 39 days: no injection.
  - From 39 to 46 days: inflow is occurred due to pressure difference (3 MPa, constant gas pressure).
  - From 46 to 71 days: a linear gas injection rate is assumed:
    - From 46 to 67 days: 0 to 1.25×10^{-8} m^3/s (1 bar was assumed).
    - From 67 to 71 days: 1.25×10^{-8} to 1.29×10^{-8} m^3/s (1 bar was assumed).
  - After 71 days: no injection.
- **Mechanical conditions**: displacements are restrained at the boundary (zero-displacement boundary).
- **Other conditions**: temperature is prescribed at 10 °C everywhere.

For experiment 2, different boundary conditions are assumed:

- **Hydraulic conditions**: water pressure is prescribed to 1 MPa at the gas injection point and at the radial filters (A and B in Fig. 32b). At these locations, water saturation is prescribed to 0 and to 0.98 respectively and flowrate is prescribed to 0 m^3/s everywhere except in these locations. Gas pressure is prescribed to 1 MPa at radial filters (B in Fig. 32b) and in the injection point is calculated assuming the ideal gas law (ignoring water and gas compressibilities, assuming a constant temperature of 20 °C).
- **Mechanical conditions**: roller-boundary condition is assumed.
- **Other conditions**: temperature is prescribed at 20 °C everywhere.

Prescribed boundary conditions in NCU/TPC-V model for experiment 1 are.

- **Hydraulic conditions**: at the backpressure filter (BC1 in Fig. 33), water pressure is prescribed to 1 MPa while gas pressure is prescribed to 2.4 MPa; at the side (BC2 in Fig. 33), a no-flux condition is prescribed; and at the injection filter (BC3 in Fig. 33) gas pressure is prescribed to the given injection gas pressure and water pressure is obtained from the capillary-vs-saturation curve with a given gas pressure.
- **Mechanical conditions**: roller conditions are prescribed at all boundaries.

whereas for experiment 2:

- **Hydraulic conditions**: at the filters (BC1 and BC3 in Fig. 34), no flux is prescribed; at the radial filters (BC2 in Fig. 34), water pressure is set to 1 MPa and gas pressure is prescribed to 2.4 MPa; and at the gas injection filter, gas pressure is prescribed to the given injection gas pressure and water pressure is obtained from the capillary-vs-saturation curve with a given gas pressure.
- **Mechanical conditions**: same conditions than for experiment 1 are prescribed.

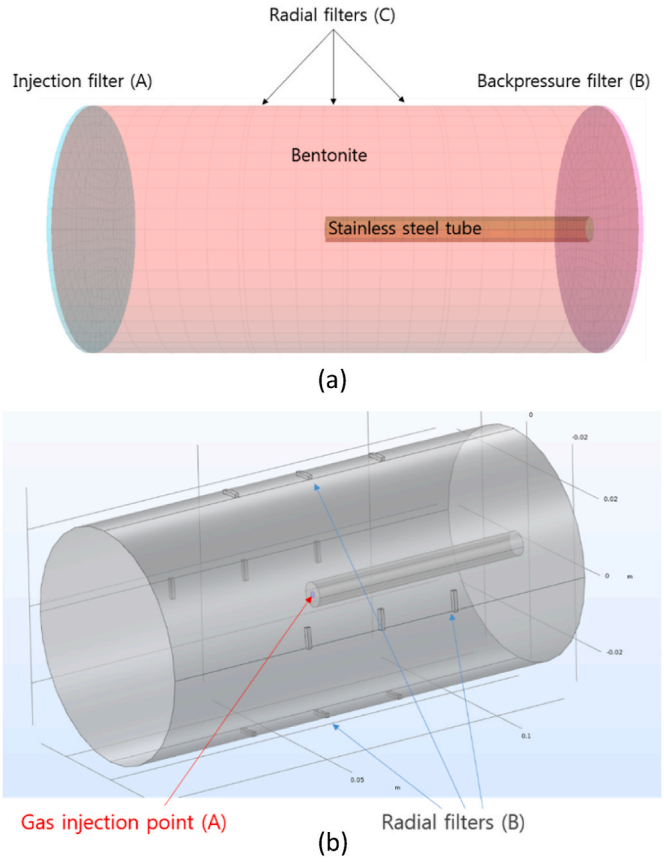

Fig. 32. KAERI-D model. Boundaries where boundary conditions are prescribed for (a) experiment 1 and (b) experiment 2.

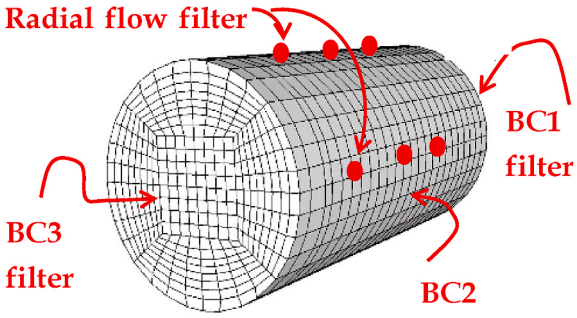

Fig. 33. NCU/TPC-V model. Locations where boundary conditions for experiment 1 are prescribed.

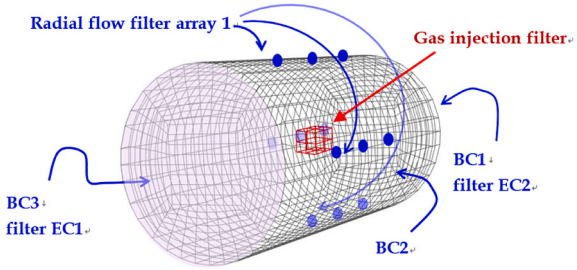

Fig. 34. NCU/TPC-V model. Locations where boundary conditions for experiment 2 are prescribed.

In UPC/Andra-ED, prescribed boundary conditions for experiment 1 are:

- **Hydraulic conditions**: water and gas pressures are prescribed at the injection surface (see Fig. 35). Indeed:
  - Water pressure is prescribed to 1 MPa throughout all the test.
  - Gas pressure is prescribed to 1 MPa from 7.4 to 39.3 days, to 3 MPa from day 40 to day 46 and released after that.
  - Gas flow rate is prescribed to 8×10^{-7} kg/s from 67 days to 71.5 days and released after that.
- **Mechanical conditions**: displacements at all axis are prescribed to 0.

Prescribed boundary conditions for experiment 2 are:

- **Hydraulic conditions**: water pressure is prescribed to 6.5 MPa at the three injection points of Fig. 35 from the day of pressurisation until day 734 and released after that; gas pressure is prescribed to 0.1 MPa at these three injection points and gas flow rate is linearly changing such that at day 736, this is equal to 1.1×10^{-10} kg/s, at day 760, this is equal to 1.8×10^{-10} kg/s and at day 835, this is equal to 1.4×10^{-10} kg/s.
- **Mechanical conditions**: displacements at the surface are prescribed to 0.

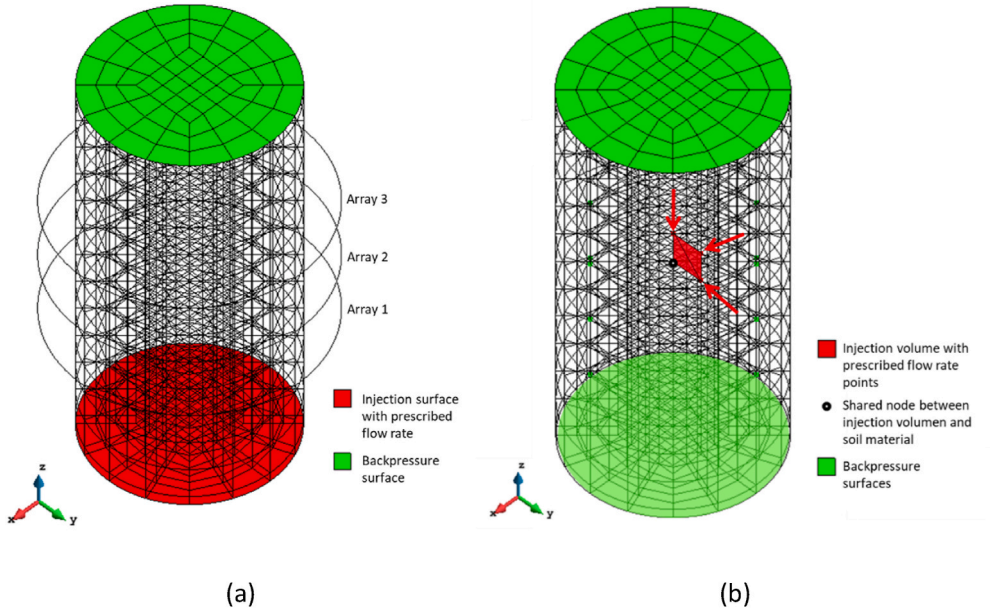

Fig. 35. UPC/Andra-ED model. Boundary conditions for (a) experiment 1 and (b) experiment 2.

As said, in experiment 1, gas flow rate was imposed at the outer edge surface of the porous stone. Different injection system volume factors were considered and several cases were run to calibrate it with a final $F_i = 15$ value assumption as the best fitting case. In experiment 2, the same strategy was followed. However, in this case, the injection was performed through an inserted surface with a single node connected to the material sample and three non-connected nodes holding the gas flow rate imposed. The same equivalent injection system volume factor as in experiment 1 was assumed.

In LBNL-D, the prescribed boundary conditions are.

- **Hydraulic conditions**: in experiment 1, at the backpressure filter, water and gas pressures are prescribed to 1 MPa and water saturation to 100%. In experiment 2, same boundary conditions are prescribed at the radial sensors (see Fig. 26).
- **Mechanical conditions**: in experiment 1, displacements are restrained at the extra padding elements. In experiment 2, same boundary conditions are prescribed at the outer chamber elements (see Fig. 26b).
- **Other conditions**: temperature is prescribed to 20 °C at the whole domain in both experiments.

In experiment 1, this model uses a huge volume to represent the injector. The injection pressure is then set to 1 MPa at the initial stage of the simulation and controlled by the injection pressure history measured in the experiment. On the contrary, in experiment 2, a constant injection rate is taken from the test and the volume of the injection element is calibrated in order to match the initial slope of the injection pressure evolution. The initial condition of injection pressure is 6.260 MPa.

Finally, in Quintessa/RWM-ECap, boundary conditions in experiment 1 are:

- **Hydraulic conditions**: at the backpressure filter (B in Fig. 36, z = 120 mm), gas pressure is prescribed to 1 MPa and at the injector filter (A in Fig. 36, z = 0 mm), gas pressure is set to

$$\begin{matrix} p_g(t_0) = 3\ MPa \\ p_g(t) from\ modelled\ injector \end{matrix} \tag{66}$$

Gas pressure gradient is prescribed to 0 at r = 30 mm (C in Fig. 36).

- **Mechanical conditions**: a roller constraint condition is applied at B and C, see Fig. 33, and the piston condition

$$\sigma_{zz} = \max\left(9.5\ MPa, p_g\right) \tag{67}$$

is prescribed at z = 0 mm (A in Fig. 36).

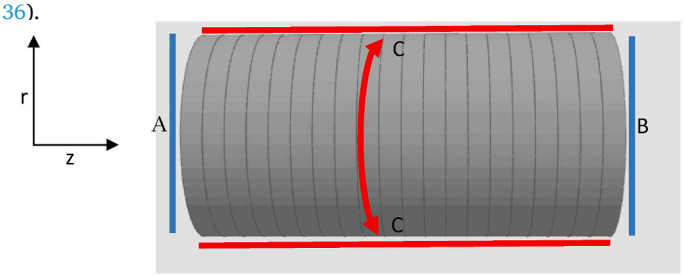

Fig. 36. Quintessa/RWM-ECap model. Boundary locations for experiment 1.

In experiment 2, boundary conditions are:

- **Hydraulic conditions**: at r = 30 mm (C in Fig. 37), gas pressure is prescribed to 1 MPa and at the injection interface (D in Fig. 37), gas pressure is set to

$$\begin{matrix} p_g(t_0) = 5\ MPa \\ p_g(t) from\ modelled\ injector \end{matrix} \tag{68}$$

Gas pressure gradient is prescribed to 0 at z = 0 mm, at z = 120 mm and at the injection rod cut-out (A, B and E respectively in Fig. 37).

- **Mechanical conditions**: a roller constraint condition is applied at A, B, C and E, see Fig. 37, and the piston condition

$$\sigma_{zz} = \max\left(7.25\ MPa, p_g\right) \tag{69}$$

is prescribed at the injection interface (D in Fig. 37).

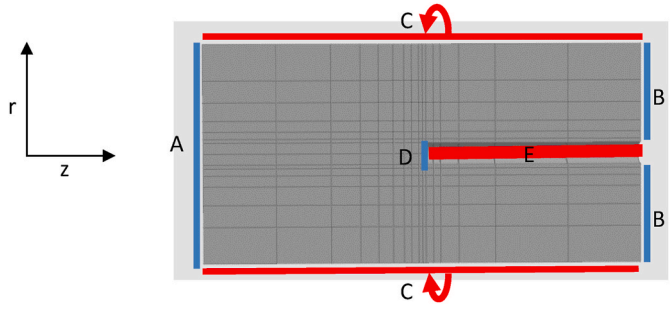

Fig. 37. Quintessa/RWM-ECap model. Boundary locations for experiment 2.

The models include an explicit representation of the injector using the ideal gas law and the prescribed gas volume changes from the experiments (i.e. refills) to calculate the gas pressure boundary condition being applied, see Table 11. For experiment 1, this is applied across the inflow end of the sample and for experiment 2, this is applied in the centre of the sample at the end of the injection rod cut-out region.

Table 11
Quintessa/RWM-ECap model: injector schedule.

Time (days)	Injection pump flow rate (uL/h)	Comments
Injector schedule for experiment 1		
39	0	Gas pressure: 3 MPa Initial gas vol.: 235 ml
46.135	500	Start of injection pump
54.149	375	Reduce injection pump flow rate
60.959	375	Gas refilled (+59.95 ml)
71.369	0	Injection pump stopped
Injector schedule for experiment 2		
720.3	125	Gas pressure: 5 MPa Initial gas vol.: 211 ml
768.3	125	Gas refilled (+91.3 ml)
799.2	125	Gas refilled (+27.6 ml)
807.4	125	Gas refilled (+61.2 ml)
827.0	125	Gas refilled (+9.3 ml)
831.1	125	Gas refilled (+47.7 ml)

Table 12
Experiment 1: boundary conditions prescribed by the participating teams.

	Model						
	BGR/UFZ-E	CNSC-PD	KAERI-D	NCU/TPC-V	UPC/Andra-ED	LBNL-D	Quintessa/RWM-ECap
Pore-water pressure (MPa)		middle, bottom and radial: no flow top and pore-fluid array boundaries: water backpressure.	backpressure and radial filters: 1	Backpressure filter: 1 Injection filter: computed from capillary-vs-saturation curve Side: no flux condition	Injection surface: 1	Backpressure filter: 1	
Pore-gas pressure (MPa)	top: 1.975 bottom: non-linear function	top and bottom: atmospheric middle: gas injection pressure radial: no flow	backpressure and radial filters: 1	Backpressure filter: 2.4 Injection filter: given injection pressure Side: no flux condition	Injection surface: 1 MPa from 7.4 to 39.3 days, 3 MPa from 40 to 46 days and released at 46.1 days	Backpressure filter: 1	Injection surface: injection history based on ideal gas law Backpressure filter: 1 At r = 30 mm, no pressure gradient (zero gas flux).
Water saturation (%)			backpressure and radial filters: 98	Injection filter: obtained from the capillary pressure-vs-saturation curve		Backpressure filter: 100	
Capillary pressure (MPa)	top: 1.875 bottom: step function						
Flowrate (kg/s)			Injection filter: step function everywhere (except injection, backpressure and radial filters): 0		Injection surface: 8 $\times 10^{-7}$ from 67 days to 71.5 days, released after that		Calculated in the model based on the injection pressure.
Displacement along x axis (m)	0	Roller constraint	0	Roller constraint	0	Extra padding elements: 0	Roller constraint
Displacement along y axis (m)	0	Roller constraint	0	Roller constraint	0	Extra padding elements: 0	Roller constraint
Displacement along z axis (m)		Roller constraint	0	Roller constraint	0	Extra padding elements: 0	Roller constraint
Stress tensor (MPa)							Injector: piston
Temperature (°C)	20		10			20	
Gas concentration		top, bottom and middle:$\rho^g(t)H(\varphi S_w)$ Radial: no flow					

Table 13
Experiment 2: boundary conditions prescribed by the participating teams.

	Model						
	BGR/UFZ-E	CNSC-PD	KAERI-D	NCU/TPC-V	UPC/Andra-ED	LBNL-D	Quintessa/RWM-ECap
Pore-water pressure (MPa)		bottom and radial: no flow top: water backpressure.	injection point: 1 radial filters: 1	Backpressure filters: no flux condition Radial filters: 1 Injection filter: computed from capillary-vs-saturation curve	3 injection points: 6.5 MPa pressurisation up to 734 days, released after that	3 radial sensors: 1	
Pore-gas pressure (MPa)	top: 1.975 bottom: non-linear function		injection point: ideal gas law radial filters: 1	Backpressure filters: no flux condition Radial filters: 2.4 Injection filter: given injection pressure	3 injection points: 0.1	3 radial sensors: 1	Injection surface: injection history based on ideal gas law At r = 30 mm, 1 top, bottom and injection rod cut-out: no pressure gradient (zero gas flux)
Water saturation (%)			Injection point: 0 radial filters: 98	Injection filter: obtained from the		3 radial sensors: 100	

(*continued on next page*)

Table 13 (*continued*)

	Model						
	BGR/UFZ-E	CNSC-PD	KAERI-D	NCU/TPC-V	UPC/Andra-ED	LBNL-D	Quintessa/RWM-ECap
				capillary pressure-vs-saturation curve			
Capillary pressure (MPa)	top: 1.875 bottom: step function						
Flowrate (kg/s)			everywhere except at gas injection point and radial filters: 0		3 injection points: 1.1×10^{-10} at 736 days, 1.8×10^{-10} at 760 days, 1.4×10^{-10} at 835 days (linearly variable)		Either from the injector model or 0 mass flux on the top, bottom and injection rod boundaries
Displacement along x axis (m)	0	Roller constraint	0	Roller constraint	0	Outer chamber elements: 0	Roller constraint
Displacement along y axis (m)	0	Roller constraint	0	Roller constraint	0	Outer chamber elements: 0	Roller constraint
Displacement along z axis (m)	0	Roller constraint	0	Roller constraint	0	Outer chamber elements: 0	Roller constraint
Stress tensor (MPa)							Injector: piston
Temperature (°C)	20		20			20	

A.5. Basic parameters

Table 14
Parameters for experiment 1.

	Model						
	BGR/UFZ-E	CNSC-PD	KAERI-D	NCU/TPC-V	UPC/Andra-ED	LBNL-D	Quintessa/RWM-ECap
Number of calibrated parameters	Not provided	25	5	7	11	Not provided	12
Elastic modulus (MPa)	307	307	307	307	307	307	307
Poisson's ratio (−)	0.4	0.4	0.4	0.4	0.4	0.4	0.4
Porosity (−)	0.44	Heterogeneity (mean: 0.44)	0.44	0.43	Heterogeneity (mean: 0.44)	0.44	Calculated
Biot's coefficient (−)	0.9	1	0.86		0.5	1	0.4
Dry density (kg/m^3)		1560	2700	1600	1512		
Intrinsic permeability of water (m^2)		3.4×10^{-21}	3.4×10^{-21}	$3.4 \times 10^{-22} \sim 3.4 \times 10^{-21}$	Heterogeneous	3.4×10^{-21}	
Intrinsic permeability of gas (m^2)							Calculated
Capillary pressure curves	van Genuchten	van Genuchten	van Genuchten	van Genuchten	van Genuchten	van Genuchten	
Relative permeability of water	Mualem	Mualem	Fatt and Klikoff [62]	Parker et al. [43]	Embedded fractures	Corey	
Relative permeability of gas	Mualem	Mualem	Fatt and Klikoff [62]	Parker et al. [43]	Embedded fractures	Corey	

Table 15
Parameters for experiment 2.

	Model						
	BGR/UFZ-E	CNSC-PD	KAERI-D	NCU/TPC-V	UPC/Andra-ED	LBNL-D	Quintessa/RWM-ECap
Number of calibrated parameters	Not provided	25	5	7	11	Not provided	12
Elastic modulus (MPa)	307	307	307	307	307	307	307
Poisson's ratio (−)	0.4	0.4	0.4	0.4	0.4	0.4	0.4
Porosity (−)	0.44	Heterogeneous (mean: 0.44)	0.44	0.43	Heterogeneous (mean: 0.44)	0.44	Calculated
Biot's coefficient (−)	0.6	1	0.86		0.5		0.3

(*continued on next page*)

Table 15 (*continued*)

	Model						
	BGR/UFZ-E	CNSC-PD	KAERI-D	NCU/TPC-V	UPC/Andra-ED	LBNL-D	Quintessa/RWM-ECap
Dry density (kg/m^3)		1560	2700	1600	1512		
Intrinsic permeability of water (m^2)		3.4×10^{-21}	3.4×10^{-21}	3.4×10^{-22}~3.4×10^{-21}	Heterogeneous	3.4×10^{-21}	
Intrinsic permeability of gas (m^2)							Calculated
Capillary pressure curves	van Genuchten	van Genuchten	van Genuchten	van Genuchten	van Genuchten	van Genuchten	
Relative permeability of water	Mualem	Mualem	Fatt and Klikoff[62]	[43]	Embedded fractures	Corey	
Relative permeability of gas	Mualem	Mualem	Fatt and Klikoff[62]	[43]	Embedded fractures	Corey	

References

1 Rodwell WR, Harris AW, Hors, Pruess K. *Gas Migration and Two-phase Flow through Engineered and Geological Barriers for a Deep Repository for Radioactive Waste.* European Commission; 1999. Report EUR19122EN.

2 Ortiz L, Volckaert G, Mallants D. Gas generation and migration in Boom Clay, a potential host rock formation. *for nuclear waste storage in Engineering Geology*. 2002; 64:287–296. https://doi.org/10.1016/S0013-7952(01)00107-7.

3 Weetjens E, Sillen X. In: *Gas Generation and Migration in the Near Field of a Supercontainer-Based Disposal System for Vitrified High-Level Radioactive Waste in Proceedings of the 11th International High-Level Radioactive Waste Management Conf.* 2006 (IHLRWM), Las Vegas, Nevada, USA, April 30 – May 4.

4 Wikramaratna RS, Goodfield M, Rodwell WR, Nash PJ, Agg PJ. *A Preliminary Assessment of Gas Migration from the Copper/Steel Canister.* Stockholm, Sweden: Svensk Kärnbränslehantering AB (SKB); 1993. Report TR-93-31.

5 Marschall P, Horseman ST, Gimmi T. Characterisation of gas transport properties of the Opalinus Clay, a potential host rock formation for radioactive waste disposal in Oil & Gas Science and Technology. *Revue de l'Institute Frances Petrole.* 2005;60: 121–139. https://doi.org/10.2516/ogst:2005008.

6 Angeli M, Soldal M, Skurtveit E, Aker E. Experimental percolation of supercritical CO2 through a caprock in. *Energy Procedia.* 2009;1:3351–3358. https://doi.org/10.1016/j.egypro.2009.02.123.

7 Cuss RJ, Harrington JF, Noy DJ, Graham CC, Sellin P. Evidence of localised gas propagation pathways in a field-scale bentonite engineered barrier system: results from three gas injection tests in the Large Scale Gas Injection Test (Lasgit). *Appl Clay Sci.* 2014;102:81–92.

8 Graham CC, Harrington JF, Cuss RJ, Sellin P. Gas migration experiments in bentonite: implications for numerical modelling. *Mineral Mag.* 2012;76(8): 3279–3292. December 2012.

9 Harrington JF, Horseman ST. In: Aplin AC, Fleet AJ, Macquaker JHS, eds. *Gas Transport Properties of Clays and Mudrocks in Muds and Mudstones: Physical and Fluid Flow Properties*. vol. 158. London: Geological Society of London Special Publications; 1999:107–124. https://doi.org/10.1144/GSL.SP.1999.158.01.09. Geological Society of London.

10 Harrington JF, Horseman ST. *Gas Migration in KBS-3 Buffer Bentonite: Sensitivity of Test Parameters to Experimental Boundary Conditions. Report TR-03-02.* Stockholm, Sweden: Svensk Kärnbränslehantering AB (SKB); 2003.

11 Harrington JF, Graham CC, Cuss RJ, Norris S. Gas network development in a precompacted bentonite experiment: evidence of generation and evolution in Applied Clay Science. 2017;147:80–89. https://doi.org/10.1016/j.clay.2017.07.005.

12 Harrington JF, Cuss RJ, Talandier J. Gas transport properties through intact and fractured Callovo-Oxfordian mudstones in Rutter. In: Mecklenburgh JEH, Taylor KG, eds. *Geomechanical and Petrophysical Properties of Mudrocks*. Geological Society of London Special Publications; 2017:454. https://doi.org/10.1144/SP454.7.

13 Horseman ST, Harrington JF, Sellin P. Gas migration in Mx80 buffer bentonite in Materials. *Research Society Proceedings*. 1996;465:1003–1010. https://doi.org/10.1557/PROC-465-1003.

14 Horseman ST, Harrington JF, Sellin P. *Gas migration in clay barriers in Engineering Geology*. 1999;54(1-2):139–149. https://doi.org/10.1016/S0013-7952(99)00069-1.

15 Horseman ST, Harrington JF, Sellin P. Water and gas flow in Mx80 bentonite buffer clay in Materials. *Research Society Proceedings*. 2004;807:715–720. https://doi.org/10.1557/PROC-807-715.

16 Bond A, Chittenden N, Thatcher K. *RWM Coupled Processes Project: First Annual Report for DECOVALEX-2019. Quintessa Report to RWM. QRS-1612d-R1 v1.2.* UK: Quintessa Ltd., Henley-on-Thames; 2018.

17 Damians IP, Olivella S, Gens A, Talandier J. *Stage 3A: Gas Flow in Natural Material: Triaxial Test on Callovo-Oxfordian Claystone.* 2019. Decovalex report.

18 Tamayo-Mas E, Harrington JF, Ivella S. *Numerical Modelling of Gas Flow in a Compact Clay Barrier for DECOVALEX-2019 in Proceedings of the Second International Discrete Fracture Network Engineering Conference.* Seattle, WA, USA: ARMA; 2018:20–22. June 2018.

19 Tamayo-Mas E, Harrington JF, B, Ivella S. *DECOVALEX-2019 Project: Task A - modElliNg Gas INjection ExpERiments (ENGINEER).* Nottingham, UK: British Geological Survey; 2018:36. OR/18/049.

20 Daniels KA, Harrington JF. *The response of compact bentonite during a 1D gas flow test.* British Geological Survey Open Report; 2017:19. OR/17/067.

21 Harrington JF, Graham CC, Cuss RJ, Norris S. *Gas Network Development in Compact Bentonite: Key Controls in Geofluids*. vol. 2019. 2019. https://doi.org/10.1155/2019/3815095. Article ID 3815095.

22 Biot MA. General theory of three-dimensional consolidation in. *J Appl Phys*. 1941;12 (2):155–164. https://doi.org/10.1063/1.1712886.

23 van Genuchten MT. A closed-form equation for predicting the hydraulic conductivity of unsaturated soils in. *Soil Sci Soc Am J*. 1980;44(5):892. https://doi.org/10.2136/sssaj1980.03615995004400050002x, 1980.

24 Mualem Y. A new model for predicting the hydraulic conductivity of unsaturated porous media in Water Resources. *Research*. 1976;12(3):513–522. https://doi.org/10.1029/WR012i003p00513.

25 Senger R, Lanyon B, Marschall P, Vomvoris S, Fujiwara A. Numerical modeling of the gas migration. *Test at the Grimsel Test Site (Switzerland) in Nuclear Technology*. 2008; 164(2):155–168. https://doi.org/10.13182/NT08-A4016.

26 Kolditz O, Bauer S, Zehner B. OpenGeoSys: an open-source initiative for numerical simulation of thermo-hydro-mechanical/chemical (THM/C) processes in porous media. *Environmental Earth Sciences*. 2012;67:589–599. https://doi.org/10.1007/s12665-012-1546-x.

27 Millington RJ, Quirk JP. *Permeability of porous solids in Transactions of the Faraday Society*. 1961;57:1200–1207. https://doi.org/10.1039/TF9615701200, 0.

28 Pall R, Moshenin NN. Permeability of porous media as a function of porosity and particle size distribution in. *TRANSACTIONS of the ASAE*. 1980;23(3):742–745. https://doi.org/10.13031/2013.34656.

29 Klinkenberg LJ. *The Permeability of Porous Media to Liquids and Gases in: API-41-200.* New York: American Petroleum Institute; 1941:41–200, 1941.

30 Alonso EE, Gens A, Josa A. A constitutive model for partially saturated soils in. *Geotechnique*. 1990;40(3):405–430. https://doi.org/10.1680/geot.1990.40.3.405.

31 Bishop AW, Blight GE. Some aspects of effective stress in saturated and partly. *Saturated Soils in Géotechnique*. 1963;13(3):177–197. https://doi.org/10.1680/geot.1963.13.3.177.

32 Khalili N, Khabbaz MH. A unique relationship for χ for the determination of the shear strength of unsaturated soils in. *Geotechnique*. 1998;48:681–687. https://doi.org/10.1680/geot.1998.48.5.681.

33 Fall M, Nasir O, Nguyen TS. A coupled hydro-mechanical model for simulation of gas migration in host. *sedimentary rocks for nuclear waste repositories in Engineering Geology*. 2014;176:24–44. https://doi.org/10.1016/j.enggeo.2014.04.003.

34 Tang CA, Tham LG, Lee PKK, Yang TH, Li LC. Coupled analysis of flow, stress and damage (FSD) in rock failure in. *Int J Rock Mech Min Sci*. 2002;39(4):477–489. https://doi.org/10.1016/S1365-1609(02)00023-0.

35 Suk H, Yeh GT. 3D, three-phase flow simulations using the Lagragian-Eulerian approach with adaptively zooming and peak/valley capturing scheme (LEZOOMPC). *Hydrologic Engineering, ASCE*. 2007;12(1):14–32.

36 Suk H, Yeh GT. Multiphase flow modeling with general boundary conditions and phase configuration changes using fractional flow approaches. *Comput Geosci*. 2008; 12:541–571. https://doi.org/10.1007/s10596-008-9094-x.

37 Tsai CH, Yeh GT. Retention characteristics for systems of multiple phase-fluids. *Terr Atmos Ocean Sci*. 2012;23(4):451–458. https://doi.org/10.3319/TAO.2012.0.14.01(Hy).

38 Tsai CH, Yeh GT. *An Advanced Constitutive Law in Multiphase Flow Model for Simulations in Compressible Media. Recent Advances in Hydrogeology*. American Geophysical Union; 2013:27–56. Chap. 2, 2013.

39 Liu IS. *Continuum Mechanics*. Berlin-Heidelberg: Springer-Verlag; 2002.

40 Liu IS. *A Continuum Mechanics Primer on Constitutive Theories of Materials*. Instituto de Matematica, Universidade Federal do Rio de Janeiro; 2006. Caixa Postal 68530.

41 Liu IS, Cipolatti RA, Rincon MA. Successive linear approximation for finite elasticity. *Comput Appl Math*. 2010;29(3):465–478. https://doi.org/10.1590/S1807-03022010000300008.

42 Yeh GT, Tsai CH, Liu IS. *GMech: A Geo-Mechanics Model for Finite Visco-Elastic Materials: Theoretical Basis and Numerical Approximation*. Jhongli City, Taoyuan: Graduate Institute of Applied Geology, National Central University; 2013.

43 Parker JC, Lenhard RJ, Kuppusamy T. A model for hysteretic constitutive relations governing multiphase flow 1. *Saturation-Pressure Relations in Water Resources Research*. 1987;23:2187–2196. https://doi.org/10.1029/WR023i012p02187.

44 Alonso EE, Olivella S, Arnedo D. Mechanisms of gas transport in clay barriers. *J Iber Geol*. 2006;32(2):175–196.
45 Senger R, Marschall P. *Task Force on EBS/Gas Transport in Buffer Material, Nagra Arbeitsbericht NAB 08-24*. 2008.
46 Corey AT. *The interrelation between gas and oil relative permeabilities in Producers monthly*. 1954;19(1):38–41.
47 Pruess K, Oldenburg C, Moridis G. *TOUGH2 User's Guide, Version 2*. Lawrence Berkeley National Laboratory; 2012.
48 Biot MA, Willis DG. The elastic coefficients of the theory of consolidation in. *J Appl Mech*. 1957;24:594–601.
49 Donohew AT, Horseman ST, Harrington JF. Gas entry into unconfined clay pastes at water contents between the liquid and plastic limits. In: Campbell LS, Valsami-Jones E, Batchelder M, eds. *Environmental Mineralogy – Microbial Interactions, Anthropogenic Influences, Contaminated Land and Waste Management J D Cotter-Howells*. vol. 9. London, UK: Mineralogical Society Special Publication; 2000: 369–394. https://doi.org/10.1180/MSS.9.18. Mineralogical Society of Great Britain and Ireland.
50 Pusch R, Forsberg T. *Gas Migration through Bentonite Clay*. Stockholm, Sweden: Svensk Kärnbränslehantering AB; 1983. SKB Technical Report 83-71.
51 Bond A, Chittenden N, Thatcher K. *RWM Coupled Processes Project: Second Annual Report for DECOVALEX-2019. Quintessa Report to RWM. QRS-1612d-R2 v2.1*. UK: Quintessa Ltd., Henley-on-Thames; 2019.
52 Bond A, Chittenden N, Thatcher K. *RWM Coupled Processes Project: Third Annual Report for DECOVALEX-2019. Quintessa Report to RWM. QRS-1612d-R3*. UK: Quintessa Ltd., Henley-on-Thames; 2019.
53 Wang Y, Faybishenko B, Harrington J. *Nonlinear Dynamics of Gas Migration in Water-Saturated Compacted Clay, DECOVALEX 2019 Technical Symposium in Brugg*. 2019. Switzerland, 11/04/2019 - 11/07/2019.
54 Bani-Yaghoub M. *Analysis and Applications of Delay Differential Equations in Biology and Medicine*. 2017, 04173v1. arXiv: 1701.
55 Strogatz SH. *Nonlinear Dynamics and Chaos: With Applications to Physics, Biology, Chemistry, and Engineering*. Westview; 2001.
56 COMSOL. *COMSOL Multiphysics Version 5.4a*. 2018. Manual.
57 Itasca, FLAC3D Version 6.0. *Fast Lagrangian Analysis of Continua in 3 Dimensions*. ITASCA Consulting Group Inc; 2018. https://www.itascacg.com/software/flac3d.
58 Olivella S, Gens A, Carrera J, Alonso EE. Numerical formulation for a simulator (CODE_BRIGHT) for the coupled analysis of saline media in. *Eng Comput*. 1996;13: 87–112. https://doi.org/10.1108/02644409610151575.
59 Asahina D, Houseworth JE, Birkholzer JT, Rutqvist J, Bolander JE. Hydro-mechanical model for wetting/drying and fracture development in geomaterials in. *Comput Geosci*. 2014;65:13–23. https://doi.org/10.1016/j.cageo.2013.12.009.
60 Quintessa. *QPAC: Quintessa's General-Purpose Modelling Software*; 2013. QRS-QPAC-11 http://www.quintessa.org/qpac-overview-report.pdf.
61 Bond A. *A Mechanical Module for QPAC Specification, Implementation and Testing. Quintessa Report QRS-QPAC-MECH-1 v1.0*. 2013.
62 Fatt I, Klikoff Jr W. Effect of fractional wettability on multiphase flow through porous media in. *J Petrol Technol*. 1959;11:71–76. https://doi.org/10.2118/1275-G.